AGU PUBLICATIONS

JGR

Journal of Geophysical Research: Oceans

RESEARCH ARTICLE

10.1002/2015JC011002

Key Points:
- Rapid and extensive cooling events are observed along the northern Patagonian continental shelf break
- Cooling events lead to significant increase of surface chlorophyll
- Intense shelf break upwelling events are the most likely explanation of extreme surface cooling

Supporting Information:
- Supporting Information S1

Correspondence to:
A. R. Piola,
apiola@hidro.gov.ar

Citation:
Valla, D., and A. R. Piola (2015), Evidence of upwelling events at the northern Patagonian shelf break, *J. Geophys. Res. Oceans*, *120*, 7635–7656, doi:10.1002/2015JC011002.

Received 26 MAY 2015
Accepted 26 OCT 2015
Accepted article online 30 OCT 2015
Published online 22 NOV 2015

Evidence of upwelling events at the northern Patagonian shelf break

Daniel Valla[1] and Alberto R. Piola[1]

[1]Departamento Oceanografía, Servicio de Hidrografía Naval and Departamento Ciencias de la Atmósfera y los Océanos, Facultad de Ciencias Exactas y Naturales, Universidad de Buenos Aires, and UMI/IFAECI, CONICET, Buenos Aires, Argentina

Abstract The Patagonian shelf break marks a transition between relative warm-fresh shelf waters and relative cold-salty Subantarctic Water advected northward by the Malvinas Current. From early spring to late autumn, the outer shelf region is characterized by a band of high chlorophyll concentration that sustains higher trophic levels, including significant fisheries. We analyze time series of current and water mass property observations collected at two moorings deployed at the shelf edge at 41°S and 43.8°S to investigate what mechanisms lead to temperature variability at the shelf break, and their role on the nutrient supply to the upper layer. The in situ data are combined with satellite-derived observations of sea surface temperature and chlorophyll *a* to analyze a sharp cooling event at the outer shelf that lasted 10 days and extended ~500 km along the outer shelf. The event is consistent with upwelling of cold waters through the base of the mixed layer. The vertical velocity required to explain the observed cooling is 13–29 m d^{-1}. Satellite-derived sea surface temperature reveals additional cooling events of similar characteristics. Seventy-five percent of these events are concurrent with surface chlorophyll increase over a 5 day period suggesting that cooling events observed at the shelf break are associated with nutrient fluxes that promote the growth of phytoplankton.

1. Introduction

Shelf break fronts (SBFs) mark a thermohaline transition frequently observed between relatively shallow continental shelves and the neighboring deep ocean. SBFs are characterized by high phytoplankton biomass, enhanced activity at higher trophic levels [*Longhurst*, 1998], and sustain intense fishing activity [*Heileman*, 2009]. Consequently, SBFs may also play an important role in the biogeochemical cycle of carbon of marginal seas [*Walsh*, 1991; *Muller-Karger et al*., 2005]. Improving the knowledge of the physical processes associated with SBFs is central to better understand the interaction of these regions with the surrounding ocean and their biological and biogeochemical significance.

The continental shelf off southeastern South America extends from the tip of Tierra del Fuego (55°S) to Cabo Frio (23°S) hosting one of the most productive marine ecosystems of the world ocean [*Bisbal*, 1995; *Falabella et al*., 2009]. South of about 40°S, the region is referred to as the Patagonian shelf. The Patagonian shelf is occupied by Subantarctic Shelf Water, a diluted variety of Subantarctic Water that enters the shelf mostly through its southern border and the Le Maire Strait. Salinity (S) increases offshore from <33.6 close to shore to ~33.9 near the shelf break [*Guerrero and Piola*, 1997]. The high tidal amplitudes, low-salinity water flux from the Strait of Magellan, and the persistent westerly winds force a mean northeast circulation over the Patagonian shelf [*Rivas*, 1997; *Palma et al*., 2004, 2008; *Palma and Matano*, 2012]. The region is bounded offshore by the Malvinas Current (MC), a narrow branch of the Antarctic Circumpolar Current that flows northward along the continental slope of Argentina advecting relatively cold ($T < 15$°C) and fresh ($S \sim 34.2$) Subantarctic Water [*Peterson and Whitworth*, 1989; *Piola and Gordon*, 1989; *Matano*, 1993]. Numerical models indicate that north of ~50°S, the MC controls the shelf break dynamics, the cross-shelf exchanges, and strongly influences the shelf circulation, thus modulating the mean flow over the outer shelf [*Palma et al*., 2008; *Matano et al*., 2010].

The transition between shelf and MC water is characterized by moderate cross-front temperature and salinity gradients, generally referred to as the Patagonia shelf break (PSB) front [*Romero et al*., 2006; *Saraceno et al*., 2004]. In situ and satellite observations show high chlorophyll concentrations and primary production

over the shelf break during spring and summer [*Carreto et al*., 1995; *Romero et al*., 2006; *Garcia et al*., 2008; *Lutz et al*., 2010]. This is in contrast with the sharp decrease in surface chlorophyll observed in summer in the northern midshelf region due to the combined effect of nutrient depletion during the preceding spring bloom and the development of strong vertical stratification [e.g., *Carreto et al*., 1995; *Romero et al*., 2006]. The abundant phytoplankton sustains higher trophic levels, including several economically important pelagic and benthic species [*Sánchez and Ciechomski*, 1995; *Rodhouse et al*., 2001; *Acha et al*., 2004; *Bogazzi et al*., 2005]. The substantial primary production at the shelf break [*Garcia et al*., 2008; *Lutz et al*., 2010] promotes the absorption of large quantities of atmospheric carbon dioxide [*Bianchi et al*., 2005, 2009].

The shelf break productivity requires a substantial nutrient flux to the upper layer, but the processes that mediate these fluxes are unknown. The strong linear correlation between temperature and nitrate ($r^2 = 0.97$) observed over the shelf at 38°S suggests that the MC is a significant nutrient source in the northern portions of the shelf [*Carreto et al*., 1995]. *Signorini et al*. [2009] have found a nonlinear nitrate versus temperature relationship ($r^2 = 0.93$) that holds over the shelf and neighboring deep ocean in a wide latitude range (~25°S–46°S). Thus, influx of nutrients to the outer shelf may be associated with cooling events such as those observed near 41°S, which create high peaks in surface chlorophyll *a* concentration [*Piola et al*., 2010]. It has also been hypothesized that quasi-permanent shelf break upwelling is associated with a divergence of the MC flow as a result of bottom friction over the sloping bottom, thus leading to nutrient injection to the upper layer [*Matano and Palma*, 2008]. Recently, high-resolution simulations corroborate these findings and indicate that the upwelling is modulated by the strength of the MC and is insensitive to changes in local wind forcing [*Combes and Matano*, 2014]. Nevertheless, the physical processes that lead to strong cooling, and presumably nutrient flux into the photic zone, required to sustain the growth of phytoplankton over the shelf break throughout the summer are poorly understood. The purpose of this paper is to investigate these processes by analyzing the variability of water mass properties and currents at the shelf break. Hydrographic and current meter data collected on the PSB are analyzed together with satellite-retrieved sea surface temperature (*SST*) and surface chlorophyll *a* concentration (*CSAT*). The data and methods are described in section 2. Though the study is focused primarily on processes leading to changes in the temperature distribution, to understand their relation with changes in the circulation, the results presented in section 3 include a brief description of the nature of the variability of the currents and water mass structure in the time and frequency domains. In section 4, we discuss the mechanisms leading to temperature variability and concluding remarks are presented in section 5.

2. Data and Methods

2.1. Moorings

The present study is based on the analysis of in situ data collected on two mooring deployments in the northern PSB. The moorings were deployed at the shelf break at 43.8°S from 16 October to 5 December 2005 (site A) and at 41°S from 25 September 2006 to 8 March 2007 (site B) (Figure 1 and Table 1). The mooring configuration is presented in Figure 2. It consists of an oceanographic buoy holding a set of atmospheric sensors (air temperature, humidity, and wind speed and direction). The underwater sensors include a hull-mounted Sea-Bird temperature-conductivity SBE 37-IM MicroCAT at a nominal depth of 1 m and a downward looking Nortek Continental 190 kHz acoustic Doppler current profiler (ADCP). During the first deployment at site A, temperature and conductivity were measured at five additional depth levels using Sea-Bird MicroCATs mounted on an inductive cable for real-time data transmission to the surface buoy and satellite telemetry to land (see Table 1). The system configuration during the second deployment at site B was identical except that only the hull-mounted MicroCAT was installed. Data from both sites were transmitted to land every 3 h through a satellite link and hourly data were stored on site. The present analysis is based on hourly recorded data.

At both sites, the ADCP measured the current speed and direction of nearly the full water column. Current velocity estimates are based on acoustic backscatter observations from 10 m bins and recorded at 10, 30, 50, 70, 100, 130, and 160 m. Velocity was decomposed into orthogonal long-shore (*V*) and cross-shore (*U*) components. Based on the orientation of the continental slope, the reference axes were rotated 20° and 40° from true north at sites A and B, respectively. Except for the determination of coherence and variance spectra discussed in section 3, the velocity components, temperature, and salinity data have been low-pass

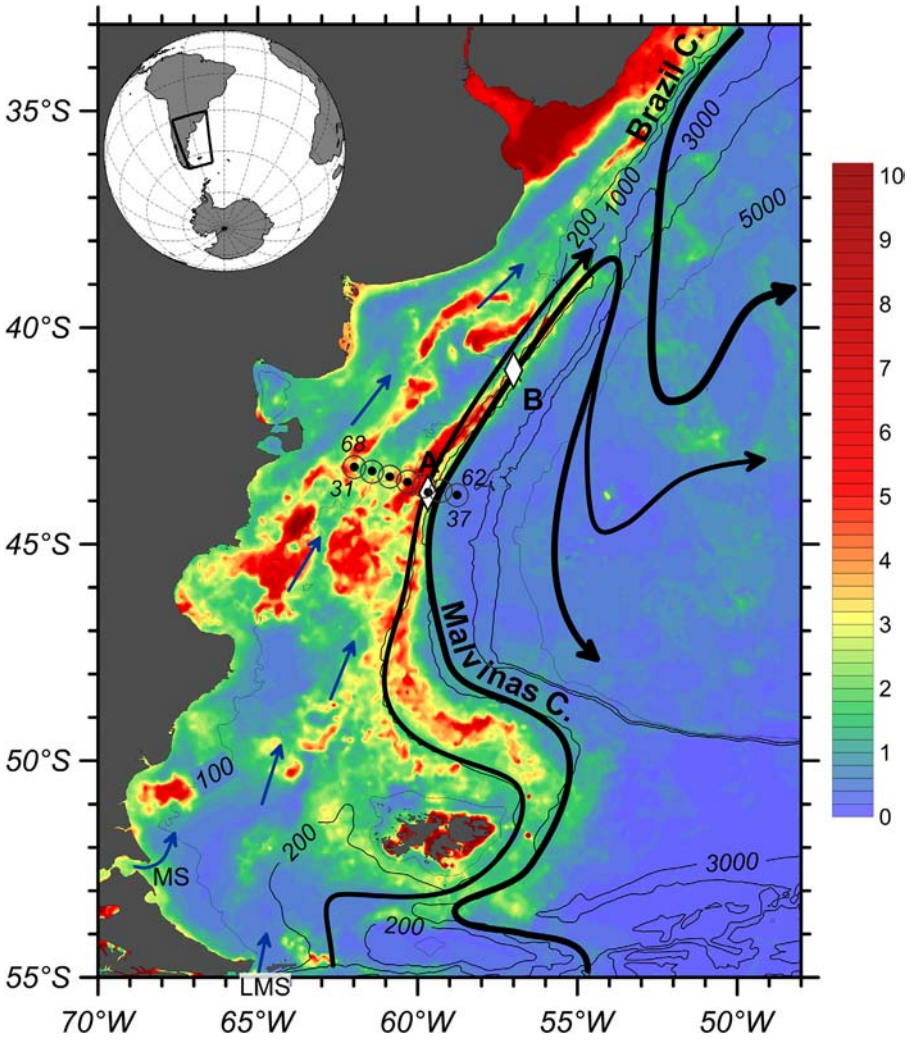

Figure 1. Location of mooring sites A and B (white diamonds) and hydrographic stations occupied in October 2005 (open circles, stations 31–37) and March 2006 (black dots, stations 62–68) used to prepare the sections shown in Figure 3. Selected station numbers are indicated. Background colors are the mean surface chlorophyll *a* from MODIS for October 2005 in mg m^{-3}. Also shown is a schematic upper ocean circulation adapted from *Piola and Matano* [2001]. Black contours represent the bottom topography in m from GEBCO [*IOC et al.*, 2003].

filtered with a cutoff period of 40 h. The filter effectively removes the strong tidal and inertial components observed in some of the original hourly records. The variability retained in the filtered data is referred to as low-frequency variability.

2.2. Hydrographic Observations

Temperature, salinity, and fluorescence cross sections are prepared based on hydrographic data obtained from CTD stations occupied during two cruises in October 2005 and March 2006. The former is coincident with the beginning of the record at site A (Figure 1). A detailed description of these observations is provided in *Charo and Piola* [2014]. The hydrographic data are available at http://data.nodc.noaa.gov/cgi-bin/iso?id=gov.noaa.nodc:0110317. In addition, we used historical hydrographic data from the US NODC World Ocean Database 2013 available at http://www.nodc.noaa.gov/OC5/WOD/pr_wod.html [*Boyer et al.*, 2013].

2.3. Satellite Observations

Satellite data are used to determine the spatial patterns of surface temperature and surface chlorophyll and their time variability. *SST* and *CSAT* data from July 2002 to December 2013 are derived from MODIS

Table 1. Statistics of Low-Pass Filtered Temperature and Salinity Measurements at Sites A and B[a]

Site	Days	Longitude/Latitude	Z (m)	$\overline{T}$ (°C)	σ_T (°C)	T_{min} (°C)	T_{max} (°C)	$\overline{S}$	σ_S	S_{min}	S_{max}
A	50.5	59.7°W/43.8°S	1	8.37	1.42	6.25	11.02	33.80	0.07	33.70	33.94
A			10	7.94	1.25	6.15	10.44	33.82	0.06	33.71	33.95
A			30	6.72	0.50	5.71	7.90	33.87	0.04	33.80	33.97
A			50	5.98	0.21	5.51	6.58	33.91	0.03	33.85	33.99
A			75	5.65	0.17	5.38	6.03	33.94	0.03	33.89	34.00
A			100	5.52	0.15	5.30	5.90	33.96	0.03	33.92	34.01
B	164	57.0°W/41.0°S	1	11.27	2.76	6.50	15.85	33.71	0.08	33.50	33.90

[a]Z: depth (m); T: temperature (°C); S: salinity; overbars indicate time average over the record length; σ denotes standard deviation; subscripts min (max) represent minimum (maximum) values recorded. See Figure 1 for site locations.

Aqua. High-resolution (twice-daily, ~1 km resolution) level 2 data (reprocessing version 2013.1.1) were processed with the standard flags and empirical algorithms (OC3M) [*O'Reilly et al*., 2000], binned, and mapped to 2 km resolution. Satellite data are distributed by the Ocean Biology Processing Group at NASA (http://oceancolor.gsfc.nasa.gov). The areal-averaged nonseasonal *SST* anomaly (*aSST*) time series presented in section 3.3.2 is based on 3 day MODIS-Aqua *SST* composites. The *aSST* was determined by subtracting the annual and semiannual cycle from the areal-averaged *SST*. In addition, and since our interest is focused on temperature changes at subseasonal time scales, to remove any additional interseasonal temperature variations, we applied a high-pass filter with a cutoff frequency of 90 days. The areal-averaged *CSAT* time series presented in section 3.3.3 is based on 3 day MODIS-Aqua *CSAT* composites. To avoid spikes due to cloud contamination, composites with more than 30% of cloud-covered pixels were excluded from the analysis. The resulting time series of *aSST* and *CSAT* contains 80% and 65% of valid data, respectively. Gaps in the time series were then filled using a cubic spline interpolation. Daily net surface heat fluxes were obtained from two sources: the Objectively Analyzed Air-sea Fluxes project (OAFlux, http://oaflux.whoi.edu/) [*Yu and Weller*, 2007; *Yu et al*., 2008] and the National Center for Environmental Prediction reanalysis (NCEP, http://www.esrl.noaa.gov/-psd/data/gridded/data.ncep.reanalysis.html) [*Kalnay et al*., 1996].

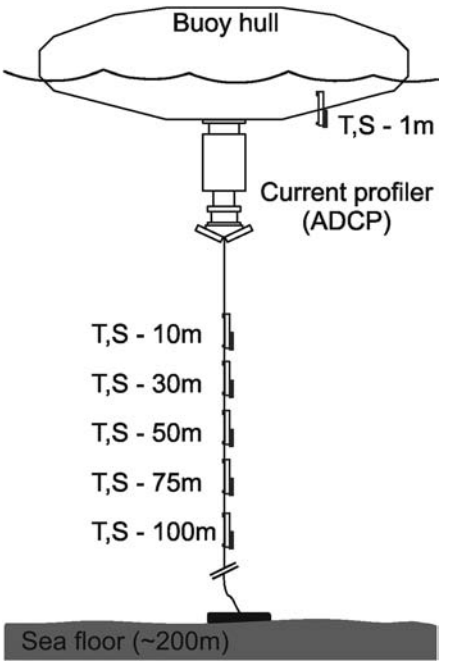

Figure 2. Mooring arrangement at sites A and B (see Figure 1 for locations). The system configuration at both sites was identical except for subsurface temperature-salinity (*T*,*S*) sensors between 10 and 100 m, which where only installed at site A.

3. Results

3.1. Thermohaline Cross-Shelf Structure

The cross-shelf thermohaline structure observed on 15–16 October 2005 near 44°S, when the mooring at site A was deployed, is illustrated in Figure 3 (see Figure 1 for station locations). Early stages of the seasonal thermal stratification are observed over the shelf, although still relatively weak compared with the summer situation [e.g., *Guerrero and Piola*, 1997, Figure 3; *Rivas and Piola*, 2002]. In October, the incipient thermocline (and pycnocline, Brunt-Väisälä frequency, $N \sim 5$ cph) is located around 50 m depth and outcrops at the outer shelf break between stations 34 and 35, creating a weak thermal front onshore of the shelf break (e.g., $\partial T/\partial x \sim -1.9$°C/100 km), and a weakening in vertical stratification ($N < 2$ cph, Figure 3a). Fluorometer data from a sensor attached to the CTD reveal high fluorescence at the shelf break, with highest concentration in the upper 50 m of the water column, and relative high concentration (>3 mg m^{-3}) extending vertically beyond 100 m depth at station 35

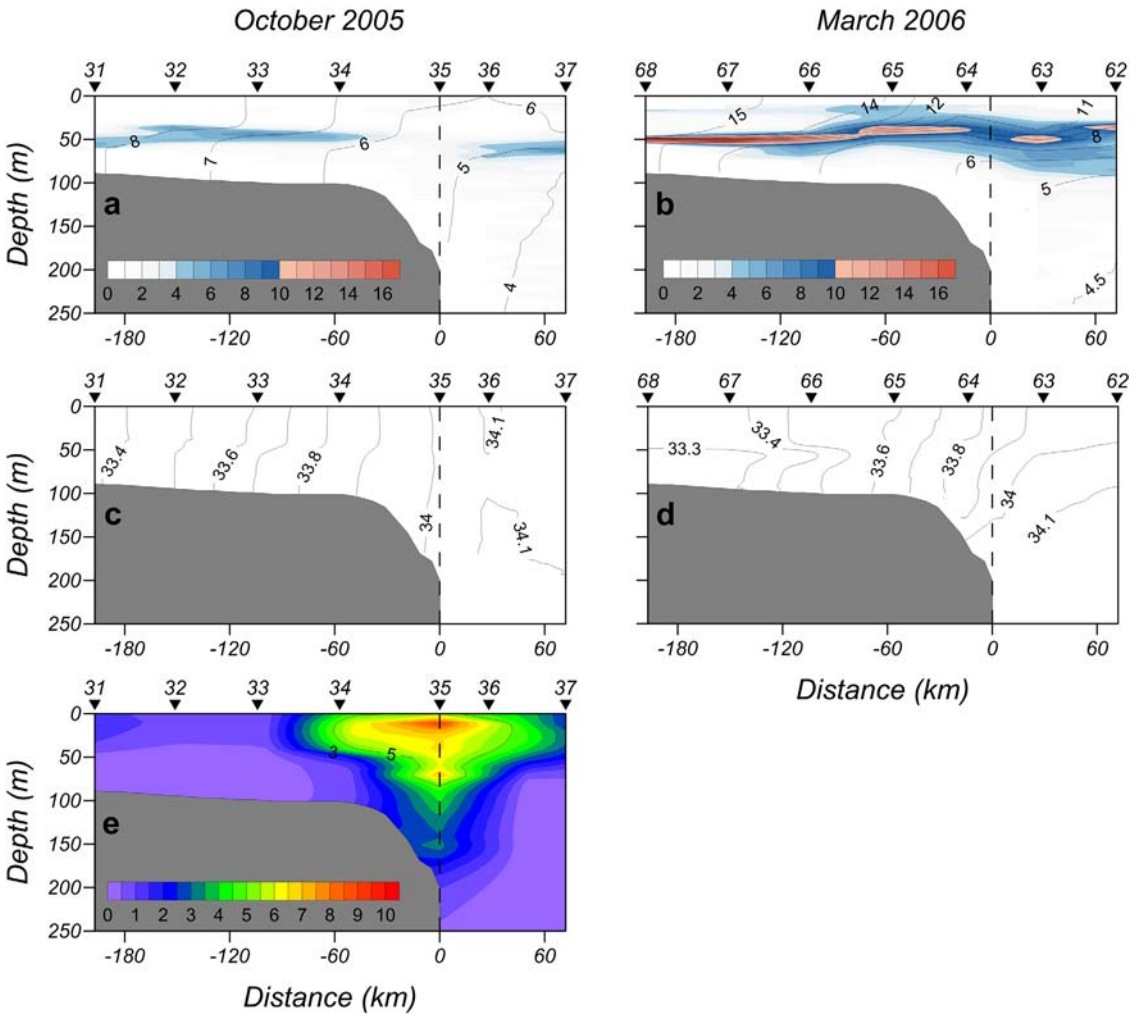

Figure 3. (top) Brunt-Väisälä frequency (cph) sections across the Patagonian shelf near 44°S collected in (a) October 2005 and (b) March 2006. Contours represent temperature in °C. (c, d) Same as Figures 3a and 3b for salinity. (e) Same as Figure 3a for chlorophyll *a* concentration (mg m^{-3}) derived from fluorescence observations. The dashed line indicates the position of site A, which is used as the origin along the distance axis. The station locations are shown in Figure 1.

(Figure 3e). Satellite-derived chlorophyll *a* suggests that this feature extends over 1200 km along the shelf break from ~50°S to 39°S (Figure 1). The data collected on 29–30 March 2006 displays a well-developed pycnocline ($N > 10$ cph), which is most intense in the midshelf region (e.g., station 67, $N \sim 16$ cph) in response to the sharp seasonal warming of the upper layer, and weakens offshore (Figure 3b). In agreement with previous analyses of seasonal *SST* variability [*Saraceno et al*., 2004; *Franco et al*., 2008; *Rivas and Pisoni*, 2010], the surface expression of the PSB is more intense in summer ($\partial T/\partial x > 2$°C/50 km, Figure 3b). Throughout the year, the salinity stratification over the shelf is weak as a result of a combined effect of low continental runoff, tidal mixing and convective sinking in winter, and strong wind mixing (Figures 3c and 3d) [see also *Guerrero and Piola*, 1997; *Rivas and Piola*, 2002; *Palma et al*., 2008]. However, there is a well-defined offshore salinity increase throughout the year (Figures 3c and 3d). Subantarctic Shelf Waters ($S < 33.8$) occupy the middle and outer shelf whereas Subantarctic Waters ($S > 34$), advected northward by the MC, are located offshore of the shelf break. Station 35 from the October 2005 survey, which coincides with site A, presents a nearly homogeneous water column occupied by relatively cold and salty slope waters (5.5°C $< T <$ 6°C; $S \sim 34$, Figures 3a and 3b).

3.2. Vertical Structure and Time Variability at the Shelf Break

3.2.1. Time Variability

In this section, we first describe the variability of temperature and velocity in the time and frequency domains at sites A and B, close to the transition between shelf waters ($S < 33.80$) and MC water ($S > 34$).

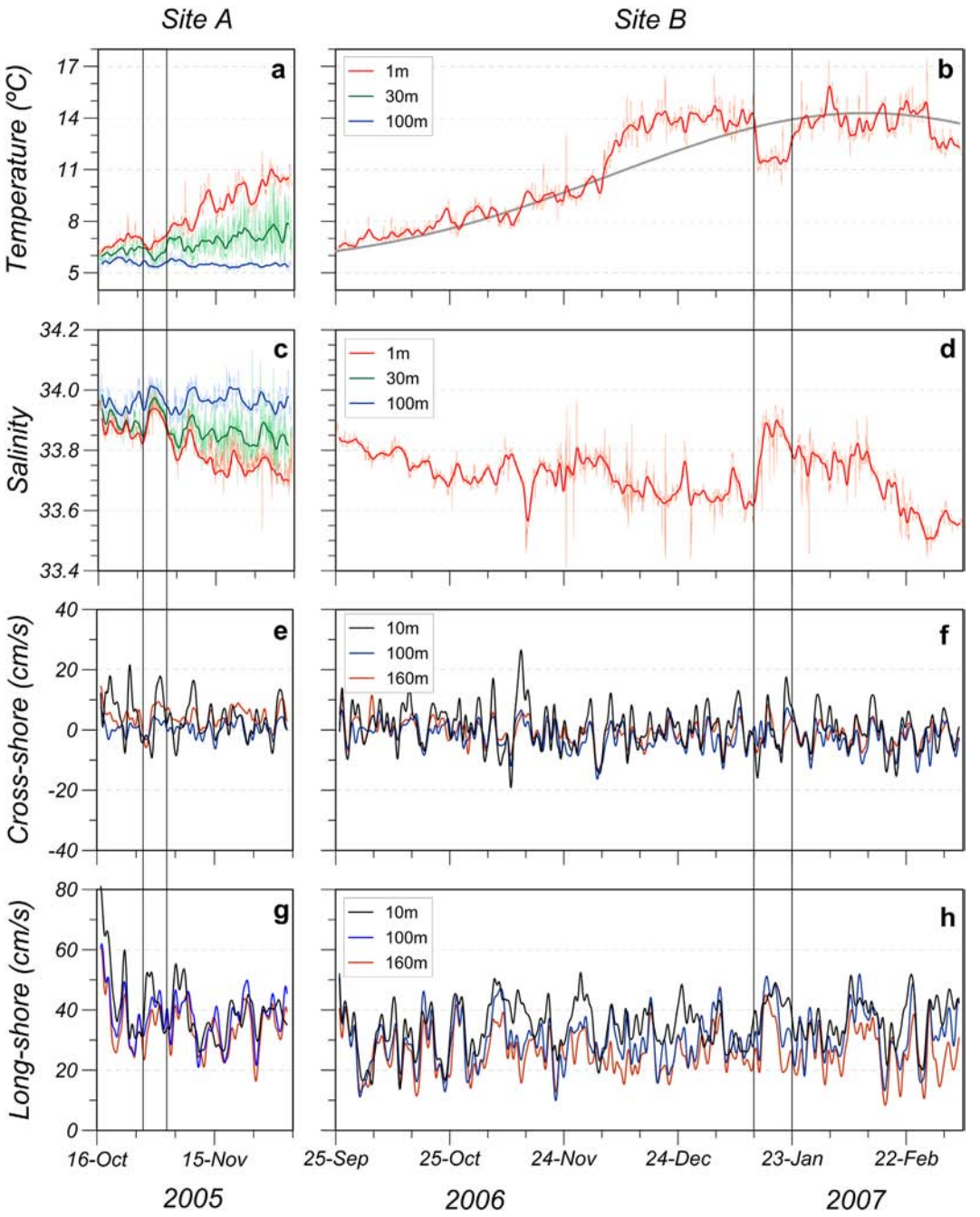

Figure 4. (top) Temperature records at selected levels at (a) site A and (b) site B. Thin (thick) lines represent unfiltered (filtered) data. The gray line in Figure 4b shows the annual cycle of satellite-derived *SST* at site B used to estimate temperature anomalies in Figure 10 (see text). (c, d) Same as Figures 4a and 4b for salinity. (e, f) Same as Figures 4a and 4b for the cross-shore velocity (positive indicates offshore current). (g, h) Same as Figures 4a and 4b for the long-shore velocity (positive indicates equatorward current). The vertical lines indicate the period of the cooling events discussed in section 3.3. Locations of sites A and B are shown Figure 1.

Figure 4 presents the *T*, *S*, *U*, and *V* time series at sites A and B from selected levels representing the upper (1 m), intermediate (30 m), and deep layers (100 m). Aside from the progressive seasonal warming displayed in the upper layer in spring, the data at both sites present significant fluctuations, particularly in both velocity components. At site A, the upper 100 m of the water column exhibits a weak thermal stratification from October until early November when the seasonal thermocline develops (Figures 4a and 5a). The base of the mixed layer stabilized at ~10 m in mid-November and presented vertical displacements of only a few meters during the remaining of the record. Virtually no net warming was observed at depths >50 m,

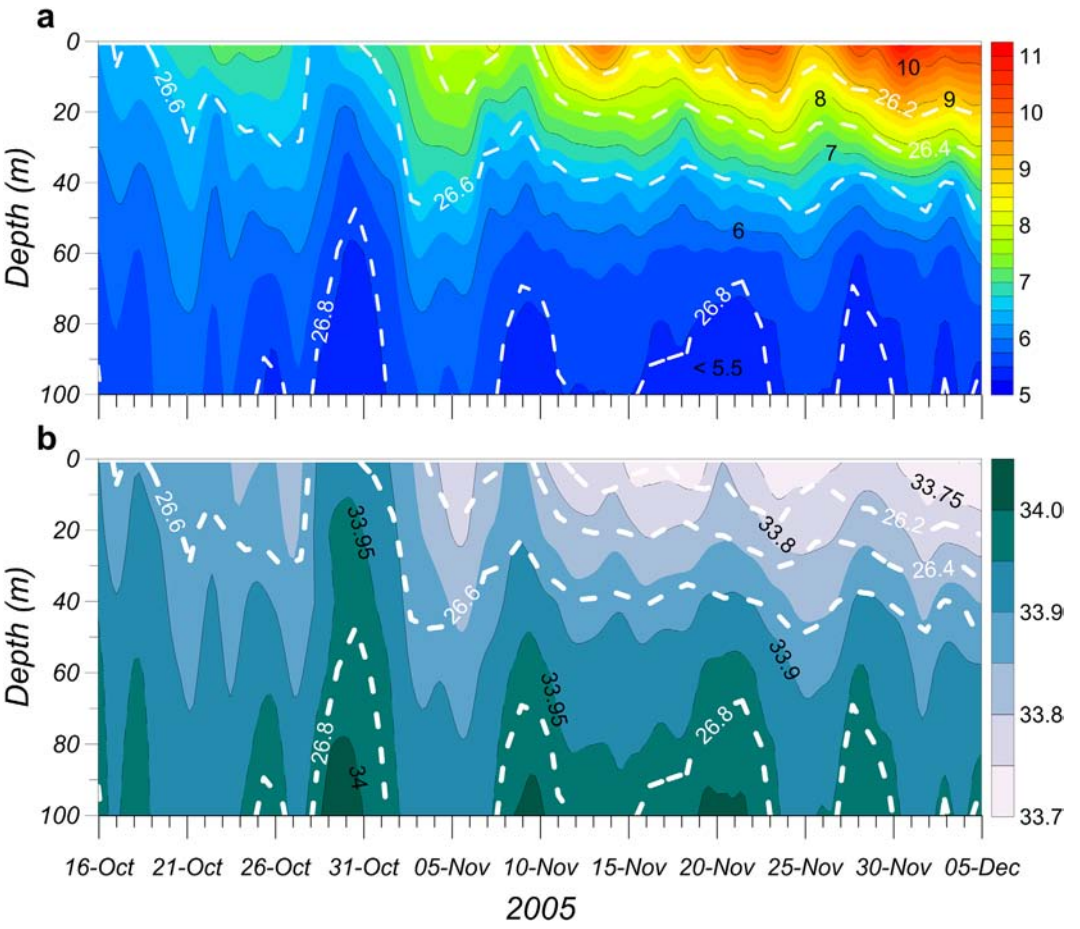

Figure 5. Depth-time distribution of (a) temperature (°C) and (b) salinity recorded at site A during October–December 2005. White dashed lines are sigma-0 contours. Location of site A is shown in Figure 1.

suggesting an increasing decoupling between the upper and lower levels from midspring onward. Record length averaged salinity increases from 33.80 at the surface to 33.96 at 100 m (Table 1), in agreement with the weak vertical salinity stratification at the shelf break indicated by the hydrographic data (Figures 3c and 3d). The upper 30 m exhibited a vertically coherent freshening of ~ -0.0031 day^{-1}, whereas no trend was detected at 100 m (Figure 4c). In addition, vertically coherent T and S pulses at $\sim$10 day intervals are observed (Figures 4a and 4c). The amplitude of these fluctuations is $\sim$1°C and 0.1 in the upper 30 m and decays to $\sim$0.4°C and 0.04 at 100 m. These salinity variations at fixed levels are associated with large vertical oscillations of isotherms and isohalines, which are particularly intense during the first half of the record (Figure 5). At 100 m, the salinity varies within the 33.75–33.95 range. Given the offshore temperature decrease and salinity increase (Figure 3), these T and S oscillations suggest intrusion of cold-salty ($<$5.5°C, $>$33.95) slope waters in the lower layers. Near-surface salinity at site B exhibited variations of 0.08 around 33.7 during most of the record (Table 1). However, in early February 2007, a progressive salinity decrease of 0.008 day^{-1} reaching minimum values lower than 33.5 was observed. To determine whether such freshening has been previously observed in the region, the historical hydrographic data from the World Ocean Database [*Boyer et al*., 2013] was inspected. We selected 77 salinity observations within the upper 30 m of the water column in the region between 40°S and 45°S, located between the 150 and 500 m isobaths and collected during January, February, and March. No water data fresher than 33.78 were found neither in summer nor throughout the year ($S > 33.707$, not shown). Thus, it is likely that the freshening observed in the last 25 days of the record at site B is at least partly due to a conductivity sensor drift.

The velocity time series from three selected levels at sites A and B show a remarkably steady and vertically coherent flow (Figures 4e–4h). Basic statistics for the upper, midlevel, and bottom ADCP velocity bins reveal that the currents are relatively intense at all levels, and somewhat weaker at site B than at site A (Table 2).

Table 2. Statistics of Low-Pass Filtered Currents for Selected Levels at Sites A and B[a]

Site	Z (m)	$\overline{U}$ (cm s^{-1})	σ_U (cm s^{-1})	U_{min} (cm s^{-1})	U_{max} (cm s^{-1})	$\overline{V}$ (cm s^{-1})	σ_V (cm s^{-1})	V_{min} (cm s^{-1})	V_{max} (cm s^{-1})	SPD_{mean} (cm s^{-1})	DIR_{mean} (°)
A	10	4	6	−9	22	40	10	26	81	41	25.6
A	70	0	2	−9	5	39	8	22	69	39	20.1
A	160	4	3	−6	14	34	8	16	61	35	27.1
B	10	1	7	−19	26	35	8	14	53	35	41.0
B	70	−2	5	−16	9	33	8	11	55	33	36.3
B	160	−1	4	−14	12	26	7	8	45	26	37.7

[a]Z: nominal depth of each selected ADCP bin; U (V): cross-shore (long-shore) velocity; overbar indicates time average over the record length; σ denotes standard deviation; subscripts min (max) represent minimum (maximum) values recorded; SPD_{mean}: time averaged speed; DIR_{mean}: time averaged velocity direction (relative to true north). See Figure 1 for site locations.

At both sites, the time averaged cross-shore component is 1–2 orders of magnitude smaller than the long-shore component, indicating that the mean flow is predominantly parallel to the bathymetry. Thus, both records indicate that the flow is strongly steered by the bottom topography, in good agreement with previous observations collected farther offshore, within the MC core [*Vivier and Provost*, 1999]. The strongest variability is observed at the surface in the cross-shore component of the current at both sites (Figures 4e and 4f). The observed mean near-surface currents at site A (∼41 cm s^{-1}) is in agreement with estimates based on Lagrangian drifters in the outer shelf near 43°S [*Piola et al*., 2013]. Direct current observations over the 1000 m isobath at 40°S present mean velocities of ∼36 cm s^{-1} at 274 dbar [*Spadone and Provost*, 2009]. The magnitude and direction of the latter observations are in agreement with near-bottom velocities (160 m) observed at site B (Table 2). *Palma et al*. [2008] compared model derived annual-averaged surface currents with the observations at sites A and B and found magnitude and direction discrepancies smaller than 10%, ascribing the discrepancy to a poor bathymetric representation of the shelf break in the model. Direct current measurements collected in the midshelf near 43°S showed significantly lower velocities than reported here, with a mean northeastward flow of ∼10 and 5 cm s^{-1} at 17 and 67 m depth, respectively [*Rivas*, 1997]. Such sharp velocity increase in the outer shelf and slope is also apparent in surface drifters [*Piola et al*., 2013] and models [*Palma et al*., 2008] and suggests that the flow at sites A and B is strongly influenced by the MC.

3.2.2. Spectral Analysis

To determine the scales dominating the time variability of the flow and thermohaline properties in the outer shelf, we estimated the spectra of the cross-shore (U) and long-shore (V) components of the current velocity and surface temperature using a fast Fourier transform. Velocity variance spectra from selected levels at site B are presented in Figure 6. Spectra from current records at all levels at site B are presented in supporting information Figure S1. The analysis is carried out on the unfiltered hourly data to retain the high-frequency variations. To increase the stability of the variance estimates, the time series were divided in 15 day pieces and averages at each frequency are presented. Spectral estimates are somewhat more reliable from observations at site B because the record is longer at that location (164 days against 52 days at site A). Though there are some spectral differences, the spectra computed at both sites for data collected during the same time of the year (from mid-October to early December, though in 2005 at site A and in 2006 at site B), and equal record lengths, are in good qualitative agreement. Thus, the results described below are generally representative of the northern shelf break region regardless of the specific location (e.g., supporting information Figures S2 and S3).

To quantify the frequency distribution of the horizontal kinetic energy, the variance of both velocity components was summed at each frequency. The total kinetic energy was then subdivided into low-frequency (periods longer than 40 h) and high-frequency band (periods between 2 and 40 h, Table 3). Table 3 also presents variance estimates for diurnal, inertial, and semidiurnal bands. At 10 m depth, both velocity components present sharp inertial, diurnal (K_1 and O_1), and semidiurnal (M_2) peaks (Figure 6a). The inertial peak, which dominates the variability at 10 m depth, decreases downward, while the energy in the semidiurnal band in the cross-shore component is vertically coherent. In addition, at both sites, the cross-shore variance at M_2 frequency is consistently higher than the long-shore variance. The velocity variance at diurnal frequency decreases at 100 and 160 m (Table 3) and the O_1 harmonic is somewhat more energetic than K_1 at 100 m for the cross-shore component and at 160 m for the long-shore component. For periods longer than 12 h at 100 and 160 m, the long-shore velocity component is more energetic than the cross-shore

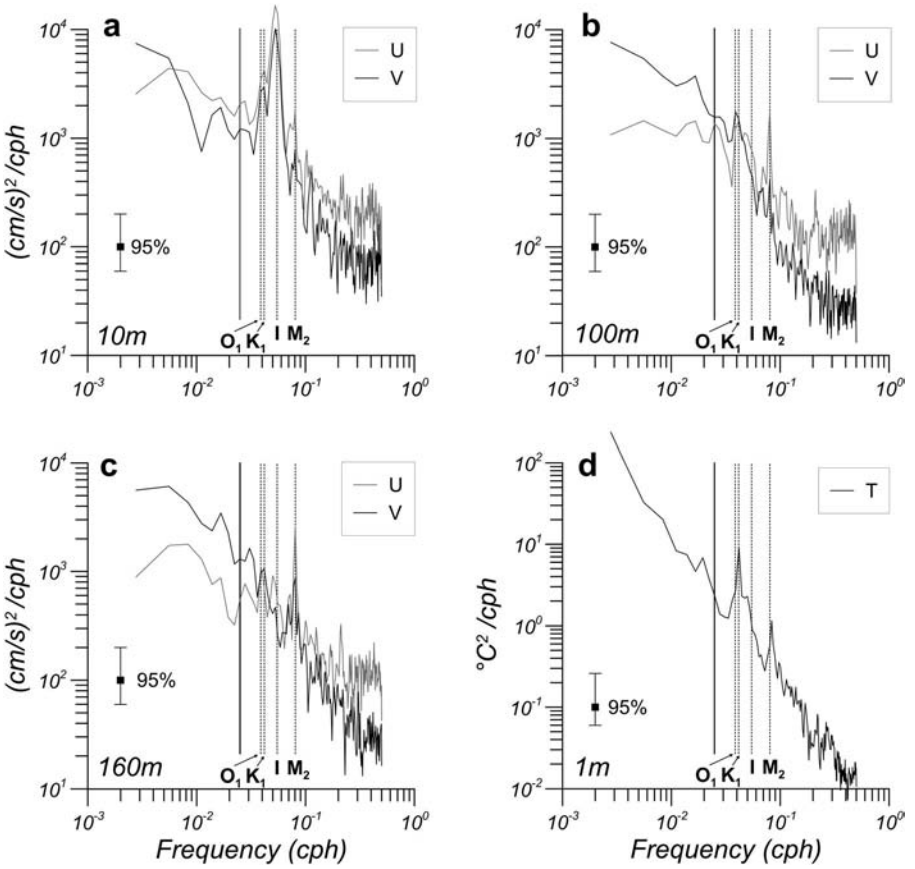

Figure 6. Spectra of currents at (a) 10 m, (b) 100 m, and (c) 160 m depth at site B. Gray lines represent the cross-shore velocity (*U*) and black lines represent the long-shore velocity (*V*). (d) Spectra of in situ temperature at 1 m depth at site B. The vertical dotted lines indicate the O_1, K_1, M_2, and inertial (I) frequencies, and the vertical solid line indicates the 40 h period, selected as limit between low-frequency and high-frequency bands (see Table 3).

component (Figures 6b and 6c). At low frequency, the variance of the cross-shore component decreases below 30 m, while the long-shore variance remains relatively high throughout the water column (Figure 6b). This cross-shore variance decrease with increasing depth is less intense at site B in the 50–100 m depth range (supporting information Figure S2). A more detailed description of the energy partition in the high-frequency bands is provided in the supporting information.

To understand the processes causing the temperature variability, particularly the strong cooling events observed at both locations (Figure 4), which presumably also lead to nutrient injection to the outer shelf, it is useful to describe the nature of the thermohaline variations. The temperature variance is high at low frequency and presents well-defined semidiurnal and diurnal peaks, particularly in the upper levels (Figure 6d and supporting information Figure S4). Though at inertial frequency, the temperature variability decays

Table 3. Temperature Variance at 1 m Depth and Kinetic Energy at All ADCP Levels at Site B[a]

		T (°C)^2	KE (cm/s)^2						
	Period Range [τ] (h)	1 m	10 m	30 m	50 m	70 m	100 m	130 m	160 m
Total fluctuating energy		1.49	327	175	162	159	145	134	132
Low-frequency energy	($\tau > 40$)	1.37 92%	64 20%	49 28%	55 34%	58 37%	60 41%	60 45%	52 39%
High-frequency energy	($\tau < 40$)	0.12 8%	263 80%	126 72%	108 66%	100 63%	85 59%	75 55%	80 61%
Diurnal subband	($22.5 < \tau < 25.7$)	0.03 2%	18 6%	7 4%	8 5%	9 6%	8 6%	6 4%	5 4%
Inertial subband	($17.1 < \tau < 18.9$)	0.01 0%	57 17%	14 8%	6 4%	5 3%	3 2%	2 1%	2 2%
Semidiurnal subband	($12 < \tau < 12.86$)	0.00 0%	6 2%	7 4%	6 4%	6 4%	4 3%	5 4%	7 5%

[a]*T*: temperature variance; *KE*: kinetic energy. Percentages represent the contribution of selected time scale ranges to the total fluctuating energy. See Figure 1 for site location.

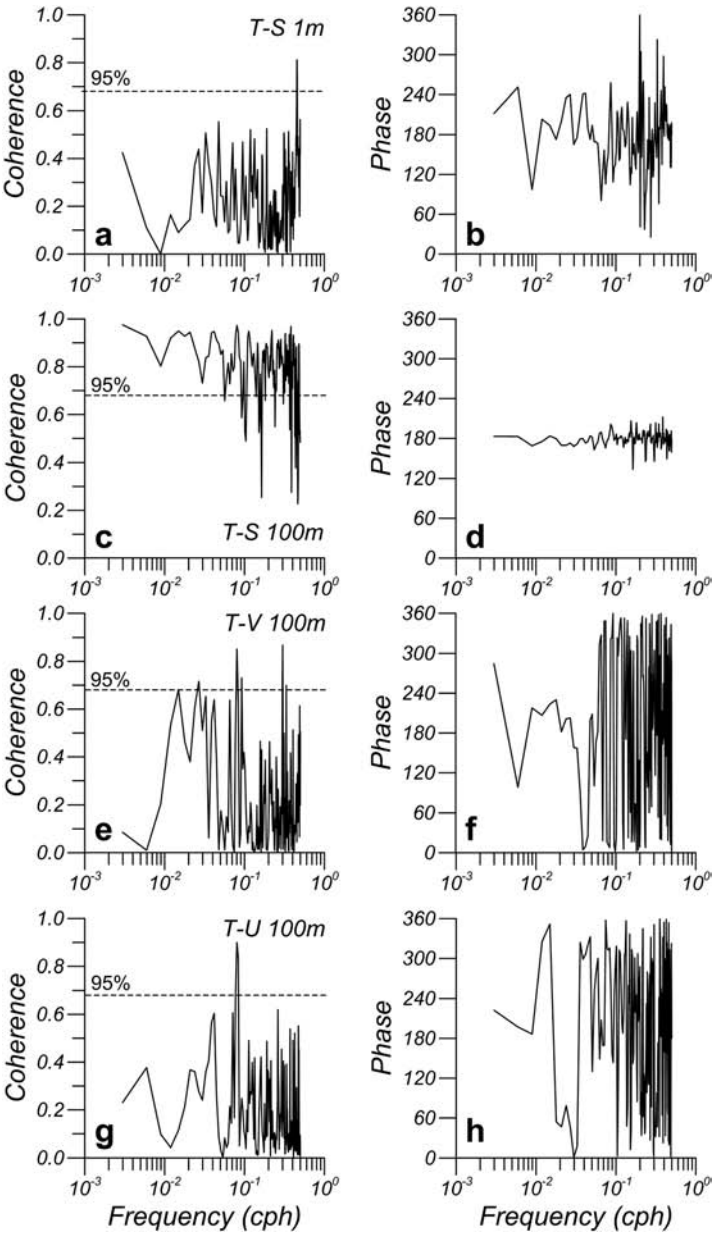

Figure 7. Coherence and phase lag spectra between temperature and salinity at (a, b) 1 m depth and (c, d) 100 m depth. Coherence and phase lag spectra between temperature and (e, f) long-shore velocity (*T-V*) and (g, h) cross-shore velocity (*T-U*) at 100 m depth. The horizontal dashed line in the coherence plots indicates the 95% confidence level.

sharply below 10 m, it is relatively high at diurnal (K1) and semidiurnal frequencies (Figure 6d). As will be shown below, the semidiurnal cross-shore velocity fluctuations are highly coherent with the temperature variability at all depths.

To better understand the nature of the shelf break variability, it is also relevant to examine the relationship between temperature and salinity variations. The coherence and phase spectra at 1 m and at 100 m depth are presented (Figure 7). No significant coherence is observed at the surface (Figure 7a). This observation indicates that recurrent surface temperature and salinity variations are produced by uncoupled processes, most likely in response to surface heat and freshwater fluxes. As will be shown later, this is in contrast with large amplitude events during which near-surface salinity fluctuations are clearly associated with temperature fluctuations at low frequency. Below 50 m depth and at periods longer than 2 days, significant coherence between temperature and salinity is observed. For example, at 100 m temperature and salinity are significantly coherent over a wide frequency range and exhibit a phase shift of $\sim$180° (Figures 7c and 7d). This is corroborated by the high anticorrelation of unfiltered *T* and *S* data at 100 m ($-$0.88). Because the shelf break marks a temperature decrease and salinity increase in the offshore direction (Figure 3), the coherent and 180° out of phase fluctuations of *T* and *S* observed below 50 m (e.g., Figure 7c) could be associated with cross-shore exchanges between warm-fresh outer shelf waters and cold-salty slope waters. To test to what extent temperature variations are correlated with local velocity variations, the coherence spectra between temperature and the two velocity components at site A were estimated (Figures 7e and 7g). Temperature fluctuations at 100 m are significantly coherent with both velocity components only at semidiurnal frequencies while coherence at other frequencies and at all levels is marginal or nonsignificant (Figures 7e and 7g). Since fluctuations of the thermohaline properties are not associated with the variability of the cross-shelf flow, except at semidiurnal frequencies, other processes must induce the observed variations at other frequencies.

3.3. Cold Events in the Outer Shelf

3.3.1. Anatomy of a Cold Event

Relatively intense and vertically coherent low-frequency *T* and *S* fluctuations are observed at both sites (Figure 4). For example, a sharp cooling (∼0.5°C) and salinity increase (∼0.1) are observed at intermediate levels at site A in late October 2005. During this event, the surface temperature and salinity dropped below 7°C and 33.9, respectively (Figures 4a and 4c). The event is associated with isotherms and isohalines rising ∼10 m d^{-1} (Figure 5). Similarly, an intense temperature decrease of ∼3°C in 2 days is observed at site B during the second half of January 2007. At this time, the salinity increased 0.27, also exceeding 33.9. This event was associated with a vertically coherent acceleration of the long-shore velocity component (Figure 4h).

Due to cloud coverage, it was not possible to examine the spatial pattern of the cooling event at site A in late October 2005 based on high-resolution satellite observations. However, inspection of infrared-based and microwave-based *SST* data (∼25 km resolution, AVHRR+AMSR) [*Reynolds et al*., 2007] confirms that the event was characterized by a relatively weak cooling rate (∼0.2°C d^{-1}). Moreover, the low-resolution *SST* data also show that the event was localized in the vicinity of the mooring site, over the area where frequent MC intrusions have been observed [*Piola et al*., 2010] (not shown). Because high-resolution satellite observations are necessary to resolve the spatial scales of the PSB front, to analyze the regional setup, we focus on the event observed at site B in mid-January 2007 (Figure 4b). MODIS *SST* composites collected before and during the event are presented in Figures 8a and 8b. South of 45°S, the *SST* patterns near the shelf break present three distinct branches of relative cold waters (*SST* < 11°C, white contour, Figure 8a). *Franco et al*. [2008] showed that low *SST* branches create multiple thermal fronts along the shelf break and within the MC. Prior to the development of the cold event, the spatial pattern of the 12.5°C isotherm (blue contour in Figures 8a and 8b) suggests that the two onshore branches converge at ∼44°S and extend north as a single cold branch to about 40°S, with its axis located offshore from the 200 m isobath. The cold event that developed after 13 January 2007 is also associated with two distinct strips of cold water (*SST* < 11.5°C), with the inshore band now extending to ∼40°S along the 200 m isobath, reaching site B (Figure 8b). The cooled region spanned the outer shelf and shelf break, although the largest cooling is centered over an elongated band extending ∼500 km along the outer shelf between 39°S and 43°S (Figure 8c). Cooling of surface water at rates higher than −0.5°C d^{-1} between the 100 and 200 m isobaths north of 43°S is associated with the presence of waters anomalously cold relative to the January climatology (*SST* < 15°C) along the outer edge of the shelf during the event (Figures 8b and 8d).

The in situ observations collected at site B and described in section 3.2.1 provide further insight on the time evolution of the cold event of January 2007. The surface temperature time series depicts the intense cooling (∼3°C) in approximately 2 days (13–15 January), in agreement with the satellite-derived *SST* rate of change for 13 January (Figures 4b and 8c). The surface waters remained relatively cold (∼11.5°C) for about a week, and warmed back to >14°C after 31 January (Figure 9a). During the low *SST* period, the surface salinity increased about 0.3, peaked at ∼33.9, and slowly decreased after the event. The near-surface cross-shore velocity was negative (onshore, ∼−13 cm s^{-1}) prior to the cooling period and positive (offshore, ∼15 cm s^{-1}) prior to its termination (Figure 9b). This suggests that cross-shore advection might be partly responsible for the cooling observed in January 2007. The cold event was also characterized by a vertically coherent acceleration of the long-shore component of the flow (Figure 9c). The highest long-shore near-bottom velocities (>40 cm s^{-1}) of the 6 months record were observed during this event (Figures 4h and 9c), with maxima exceeding 50 cm s^{-1} between 60 and 80 m depth (Figure 9c) and an average acceleration at the surface of ∼2.5 cm s^{-1} d^{-1} from 9 to 16 January. To evaluate the impact of the cooling event on surface water characteristics, in situ temperature anomalies at 1 m were determined by subtracting the annual and semiannual cycle fitted to the daily *SST* data at site B (Figure 4b). The resulting *SST* anomalies at 1 m shown in Figure 10 plotted against the 1 m salinity exhibit a general negative correlation. The largest negative *SST* anomalies are observed during the cold event of January 2007 and exhibit the highest surface salinity and deep long-shore velocity of the entire record (*S* > 33.8, *V* > 40 cm s^{-1}, Figure 10b). Though the above observations are consistent with an onshore displacement of the water mass structure and the MC core, as will be discussed in section 4, the cross-shelf flow cannot explain the temperature fluctuations observed at site B during the event.

3.3.2. Other Cooling Events

The cooling event observed on January 2007 extended over a wide part of the northern Patagonian outer shelf. To determine if similar events occur in this area, the *aSST* was estimated over a region of the northern

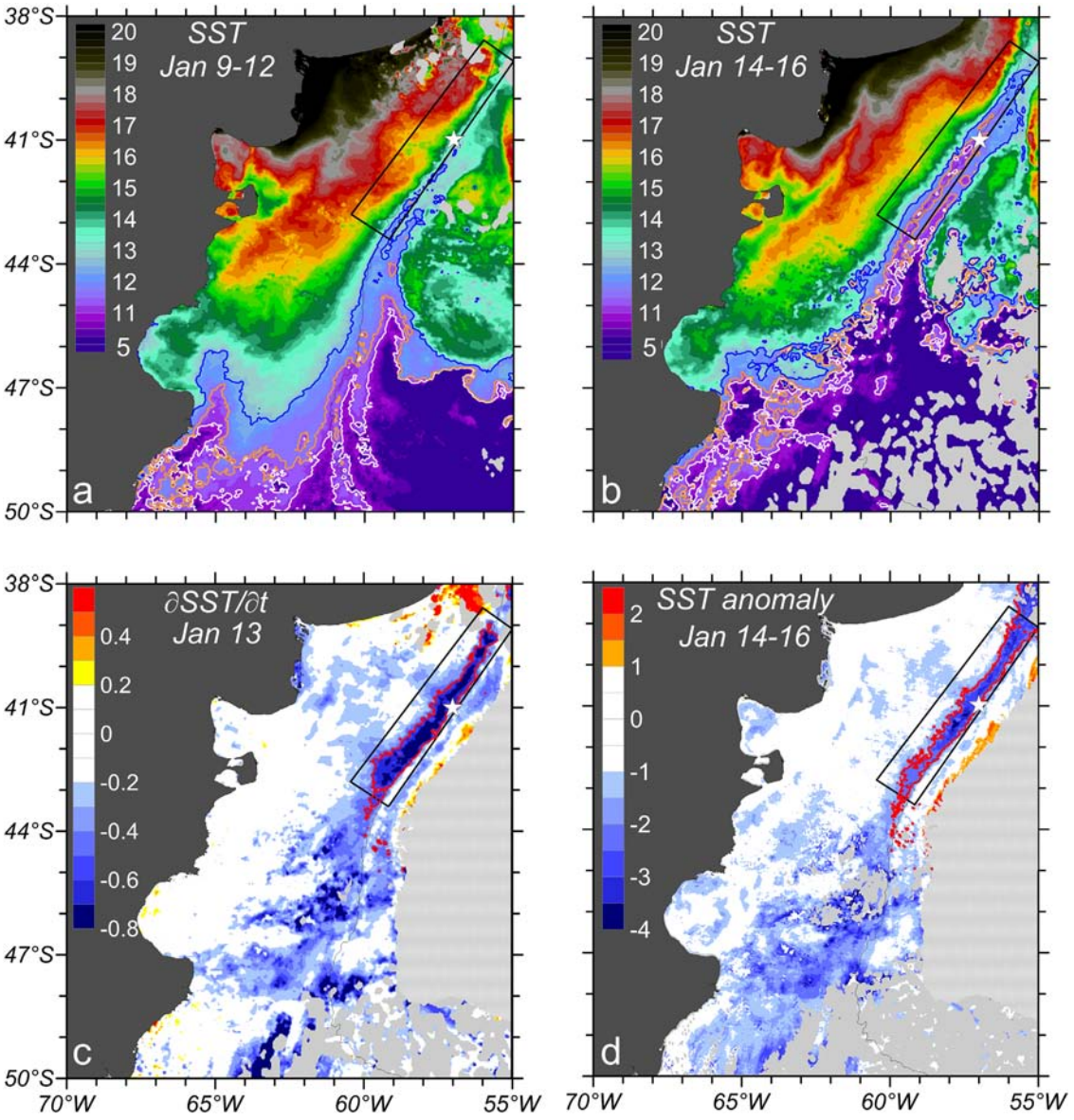

Figure 8. (a) Distribution of mean satellite-derived *SST* (°C) for the period 9–12 January 2007. (b) Same as Figure 8a for the period 14–16 January 2007. (c) *SST* rate of change (°C d^{-1}) for 13 January 2007. (d) *SST* anomalies (°C) relative to the January climatology for the period 14–16 January 2007. Blue, orange and white contours in Figures 8a and 8b represent the 12.5, 11.5, and 11°C isotherms, respectively. Red contours in Figures 8c and 8d are the 0.5°C d^{-1} and 2°C isolines, respectively. The black polygons in all panels are the region where averaged *aSST*s and *CSAT* depicted in Figure 11 were computed. Depths greater than 2000 m in Figures 8c and 8d are stippled for clarity. Light gray pixels in all panels indicate cloud-covered regions. White stars in indicate the location of site B. The solid line is the 200 m isobath from GEBCO.

portion of the outer shelf and the upper slope, between 39°S and 46°S, as detailed in section 2.3 (see Figure 8a for location). The time series of *aSST* is presented in Figure 11a. The strongest cooling events in terms of *SST* are detected from late austral spring to midfall. Thus, in Figure 11a, we only present the period from December to April for each year. Several minima associated with sharp cooling events are observed in the time series ($aSST < -1.3$°C, vertical lines in Figure 11a), including the event of mid-January 2007, which manifests itself as a local minimum ($aSST \sim -2.3$°C).

The rate of the temperature change and the magnitude and duration of each event are presented in Table 4. The duration was computed as the period during which the magnitude of (negative) *aSST* remained below 70% of the lowest *aSST* for each event. Because the heat lost to the atmosphere may have a strong impact on the evolution of the *SST* over the continental shelf [e.g., *Rivas and Piola*, 2002], Table 4 also presents the net surface heat fluxes from NCEP and OAFlux when available. The sea-air heat flux is averaged over 3 days prior

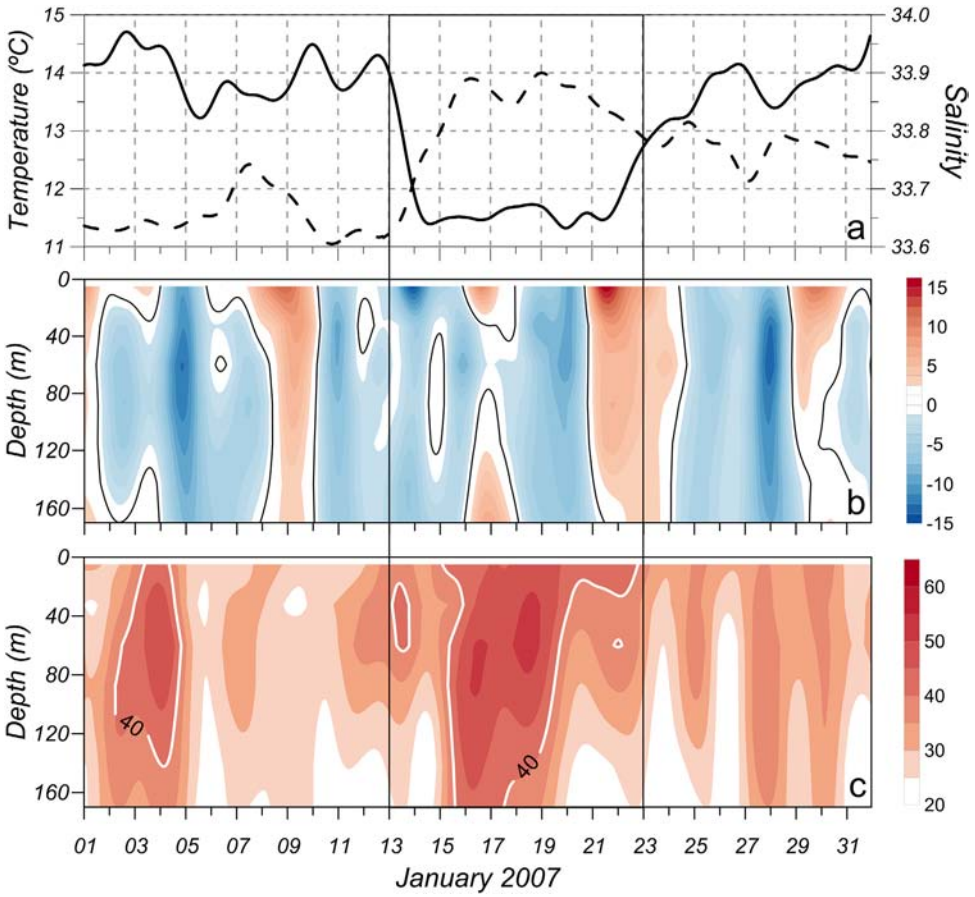

Figure 9. Low-pass filtered time series of (a) temperature (°C, solid line) and salinity (dashed line) at 1 m depth, depth-time distribution of the (b) cross-shore velocity (cm s^{-1}) and (c) long-shore velocity (cm s^{-1}) recorded at site B (see Figure 1 for location). The heavy black contour in Figure 9b indicates the 0 cm s^{-1} isotach and the heavy white contour in Figure 9c indicates the 40 cm s^{-1} isotach. The vertical lines indicate the beginning and end of the cold event described in section 3.3.1.

to each event. Although there are substantial discrepancies in the magnitude of the net heat flux between these data sets, only two events present estimates with opposite signs (events beginning on 20 January 2005 and 10 February 2008). The remaining events during which both estimates are available exhibit positive (into the ocean) net heat flux, except in April 2009. Five other events with negative NCEP net heat flux estimates are observed after 2009, although no OAFlux data are available for comparison. To investigate the spatial extent of these events, the rate of *SST* change ($\partial SST/\partial t$) of selected events was estimated using 5 day *SST* composites and mapped over the study region (Figure 12). Since two consecutive composites are necessary to produce these maps, some of the events depicted in Figure 12 cannot be displayed due to cloud contamination in either composite. All the available events present a cooling rate <-0.4°C d^{-1} in the vicinity of the shelf break and onshore of the 200 m isobath (red contour in Figure 12). The net heat flux estimates during the events are either positive or exhibit opposite signs between OAFlux, when available, and NCEP. The largest cooling rates were observed over the continental shelf and upper slope in March 2011 and March 2013. During both events, the ocean lost heat to the atmosphere at rates of 27 and 43 W m^{-2}, respectively (Table 4). Note, however, the large *SSTs* decrease over the outer shelf and upper slope ($\partial SST/\partial t < -0.8$°C d^{-1}, white contour and $\partial SST/\partial t < -1.3$°C d^{-1}, yellow contour, Figure 12). Though part of the observed cooling during these two events might be due to heat loss to the atmosphere, below we will show that this mechanism cannot explain by itself the observed cooling rate in the outer shelf.

3.3.3. Impact of Cooling Events

Subantarctic Waters advected by the MC are presumably a significant nutrient source for the relatively intense *CSAT* maxima observed in austral spring and summer along the PSB [e.g., *Carreto et al*., 1995; *Podestá*, 1997; *Romero et al*., 2006]. Therefore, the question arises as to whether the observed cooling events

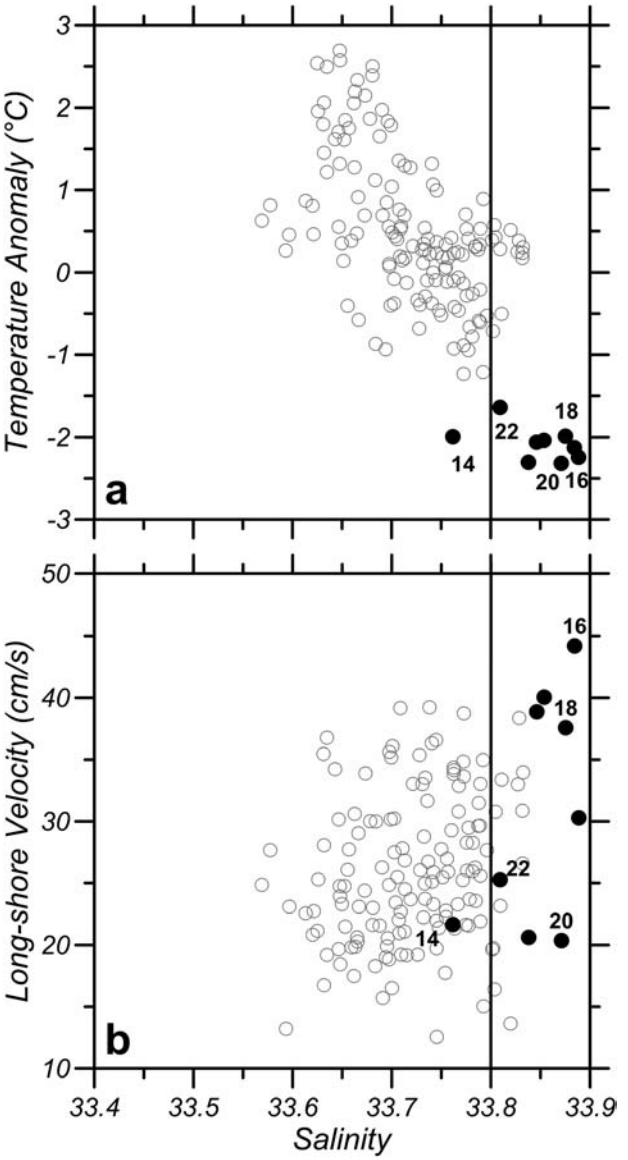

Figure 10. Diagrams of daily averaged in situ observations at site B. (a) In situ temperature anomaly (°C) versus salinity at 1 m and (b) long-shore velocity at 160 m (cm s^{-1}) versus salinity at 1 m diagrams of daily averaged in situ observations at site B (see Figure 1 for location). Black dots in both panels correspond to observations during the cold event of January 2007 (see Figure 9) and numbers indicate date of January 2007. The vertical line indicates the 33.8 isohaline which marks the shelf edge salinity.

may lead to enhanced nutrient enrichment and consequent biomass growth. To investigate this hypothesis, the areal-averaged *CSAT* was estimated over the same region where *aSSTs* were computed, as detailed in section 2.3. The time series from December to April of each year is presented in Figure 11b. Changes in *CSAT* ($\Delta CSAT$) were also determined based on a centered difference over a period of 6 days. Results are shown in Figure 11c. An increasing in *CSAT* generally follows most of the cooling events (Figures 11a and 11c), although substantial differences are observed. For example, in January 2005, a local *CSAT* maximum is observed almost simultaneously with a local *aSST* minimum, whereas a delayed response is observed after the January 2003 cooling event and no clear *CSAT* response is observed during January 2007 and March 2013. $\Delta CSAT$ associated with intense cooling events are quantified in Table 4. Finally, the spatial distribution of changes in *CSAT* concentration during selected cooling events was also analyzed. To this end, differences in *CSAT* concentration before and after each event were computed over a 10 day period using 5 day composites (Figure 12). Note that north of 38°S, near-coastal locations may have a significantly contaminated *CSAT* signal due to dissolved and suspended organic and inorganic matter derived from Plata River discharges. All events exhibit a significant increase of *CSAT* over the outer shelf (>2 mg m^{-3}, heavy black contour in Figure 12), although differences in the spatial extent of each event are observed. Interestingly, the events in which there was substantial heat loss to the atmosphere as well as enhanced cooling over the shelf break (i.e., March 2011 and March 2013) also led to noticeable *CSAT* increment over this region. It must be noted, however, that the cold event of January 2007 described in section 3.2.1 is associated with a general *CSAT* decrease in the shelf break and somewhat weaker increase in the outer shelf.

4. Discussion

4.1. High-Frequency Variability

Our results indicate that the neither the cross-shore nor the long-shore flow variability account for the local temperature and salinity variability except for fluctuations at semidiurnal tidal frequency (M_2) at 75 and 100 m (Figures 7e and 7g). The significant coherence between the cross-shore velocity and both temperature and salinity oscillations thus implies a net offshore heat flux and onshore salinity flux

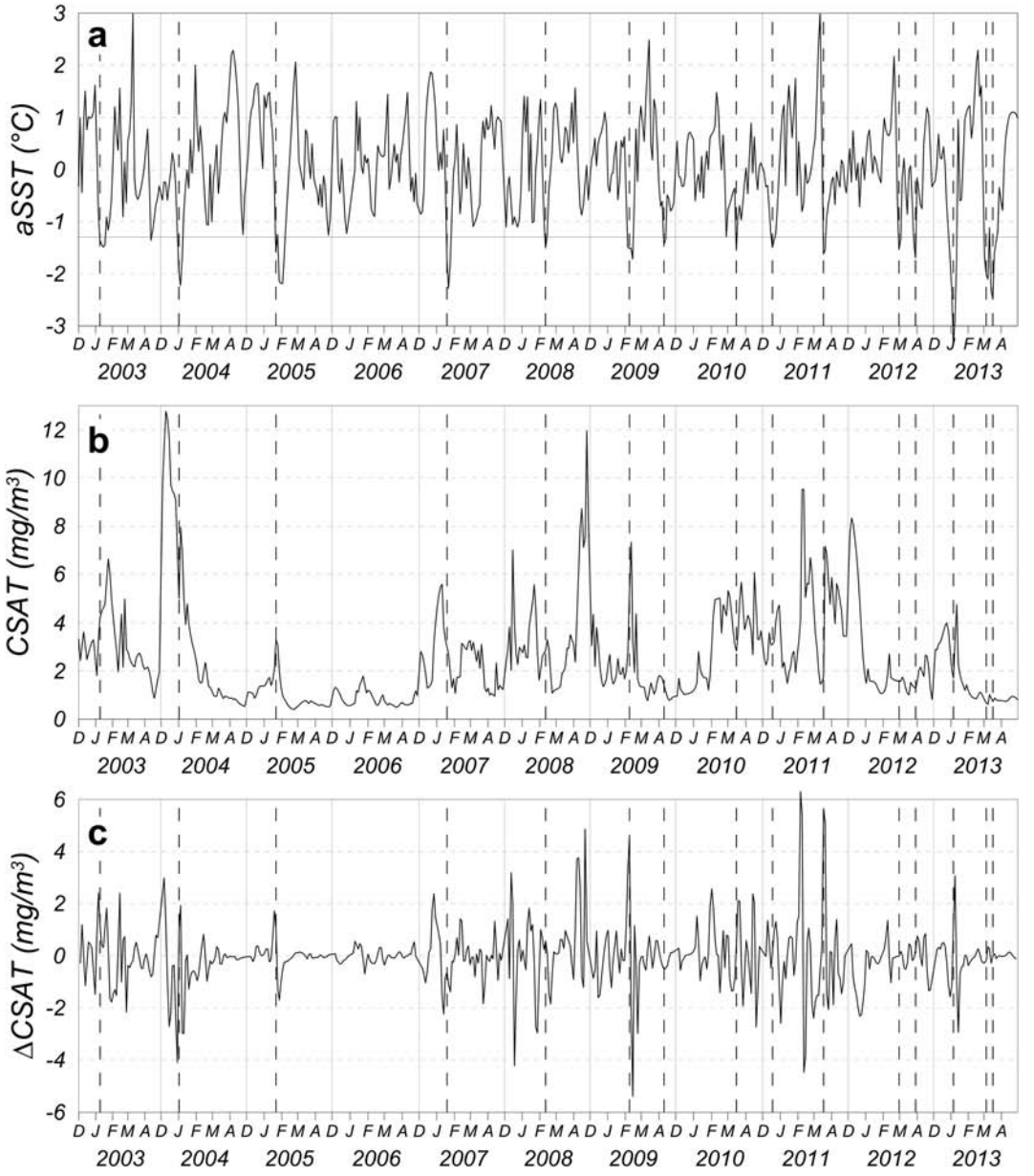

Figure 11. (a) *aSST* (°C), (b) *CSAT* (mg m^{-3}), and (c) *CSAT* difference over a 6 day period ($\Delta CSAT$, mg m^{-3}) averaged over a selected region located at the northern Patagonian shelf and shelf break (see text for description and Figure 8a for location). Only the period from December to April of each year is shown. Dashed vertical lines indicate maximum cooling events. The horizontal line in Figure 11a indicates the threshold for identifying cooling events.

below the seasonal thermocline during the observation period. The mean eddy cross-shore heat flux at 100 m associated with the M_2 frequency can be estimated as $\rho C_p \overline{u'T'}$, where $\rho = 1022$ kg m^{-3} and $C_p = 3940$ J kg^{-1} $°C^{-1}$ are the seawater density and specific heat, respectively, and $\overline{u'T'}$ is the time-averaged eddy temperature flux at 100 m due to oscillations in the M_2 frequency at site A. We obtained u' and T' by filtering the hourly time series of U and T with a band-pass filter with cutoff frequencies at 0.071 and 0.089 cph. The estimated mean eddy cross-shore heat flux associated with the semidiurnal frequency is 8700 W m^{-2}, which represents approximately 60% of the total mean cross-shore eddy heat flux at 100 m depth. Significant coherence is observed between temperature and salinity at 100 m at all time scales longer than ~18 h (Figure 7c). This is also observed at 50 and 75 m (not shown). These subsurface T and S oscillations are 180° out of phase. The in situ observations at site A also show pulses of relatively cold and salty waters throughout the upper 100 m (Figure 5). These observations are also in

Table 4. Characteristics of the Most Intense Cooling Events[a]

Date	ΔSST (°C) 6 days	ΔSST (°C) 9 days	$aSST$ (°C)	Duration (days)	Q (W m^{-2}) OAFlux	Q (W m^{-2}) NCEP	$\Delta CSAT$ (mg m^{-3}) 6 days
10 Jan 2003	**−1.49**	**−2.42**	**−1.4**	**12**	**36**	**120**	**1.1**
30 Dec 2003	**−1.21**	**−1.36**	**−1.97**	**9**	**150**	**116**	**1.0**
20 Jan 2005	**−2.10**	**−2.30**	**−1.59**	**18**	**167**	**−71**	**1.0**
16 Jan 2007	**−2.16**	**−1.20**	**−1.70**	**9**	**152**	**19**	**−0.6**
24 Nov 2007	−1.00	−0.22	−1.99	6	134	54	0.8
10 Feb 2008	**−1.34**	**−2.47**	**−1.51**	**6**	**−96**	**56**	**0.6**
18 Nov 2008	−1.44	−0.51	−1.47	9	124	87	1.7
7 Feb 2009	**−1.01**	**−2.04**	**−1.52**	**12**	**130**	**18**	**4.6**
11 Apr 2009	−1.31	−1.94	−1.45	6	−113	−91	−0.5
16 Mar 2010	−1.48	−1.54	−1.55	3		−268	0.5
14 Dec 2010	−0.16	−0.28	−1.50	12		119	0.1
17 Mar 2011	**−5.12**	**−4.75**	**−1.63**	**6**		**−27**	**5.6**
28 Feb 2012	−2.93	−4.18	−1.54	6		−15	0.0
29 Mar 2012	−1.70	−2.69	−1.69	6		−80	0.2
2 Jan 2013	−1.30	−1.56	−3.35	6		50	1.2
3 Mar 2013	**−2.20**	**−3.77**	**−2.01**	**9**		**−43**	**−0.2**
15 Mar 2013	−1.63	−0.75	−2.47	3		−99	0.0

[a]ΔSST: *SST* changes (°C) over 6 and 9 days periods; *aSST*: nonseasonal *SST* anomalies (°C); *Q*: net surface heat flux (W m^{-2}) from OAFlux and NCEP averaged over 3 days prior to each date; $\Delta CSAT$: surface chlorophyll difference (mg m^{-3}) over a 6 days period. Events indicated in bold are depicted in Figure 12.

agreement with numerical models results that suggest the existence of a cross-shelf circulation pattern dominated by upwelling and onshore subsurface intrusions of cold and dense MC water in the outer shelf [*Matano et al*., 2010].

4.2. Physical Mechanisms Associated With Low-Frequency Cooling Events

The cold event of mid-January 2007 was characterized by a simultaneous surface cooling of ∼1°C over the middle shelf and a more intense surface temperature decrease (<−2°C) in approximately 4 days over the outer shelf (Figure 8c). To investigate to what extent the cooling in these regions is associated with the same process, we analyze the atmospheric conditions during the event. Figure 13a depicts the atmospheric circulation on 13 January 2007, 1 day before the onset of the cooling event. The pressure and wind fields are derived from the Climate Forecast System Reanalysis (CSFR; http://cfs.ncep.noaa.gov/cfsr/) [*Saha et al*., 2010] and Quickscat, respectively. A low-pressure system centered on (58°S, 51°W) and a high-pressure system located west of South America generated an intense zonal atmospheric pressure gradient, and strong southerly winds (>10 m s^{-1}) over the outer Atlantic Patagonian Shelf. This is a distinctive pattern of the year-round atmospheric circulation which causes frequent incursions of cold air in the lee side of the Andes [*Garreaud*, 1999, 2000]. One consequence of the outbreak of cold air is a significant decrease of the otherwise large midsummer net heat flux into the ocean. In January 2007, the outbreak of cold air caused a reduced heat gain over the shelf north of 46°S ($Q < 100$ W m^{-2}, Figure 13b). Note that the extended region where heat is lost to the atmosphere is over the southward extension of the Brazil Current, and not over the shelf. Thus, the atmospheric event was not strong enough to overcome the large incoming solar radiation, and the net heat flux over the shelf was into the ocean, except for a narrow band close to shore near 40°S (Figure 13b). The net surface heat flux from NCEP presents a somewhat more extended region of heat loss to the atmosphere over the continental shelf (∼50 W m^{-2}, not shown). As will be shown below, this heat loss to the atmosphere would be insufficient to produce the observed cooling. Since the surface heat flux cannot explain the temperature evolution, other processes, such as mixing and advection, must play significant role in the heat balance [e.g., *Rivas and Piola*, 2002].

Over the region where maximum cooling at the outer shelf occurred, between 39°S and 43°S, positive net heat flux is observed ($Q > 100$ W m^{-2}, Figure 13b). Although enhanced vertical mixing in response to the strong southerly winds may partially explain the sharp surface cooling in this area, the noticeable asymmetry in the intensity of the cooling rates (Figure 8c) suggests that other physical processes must play a significant role in the temperature balance in the outer shelf.

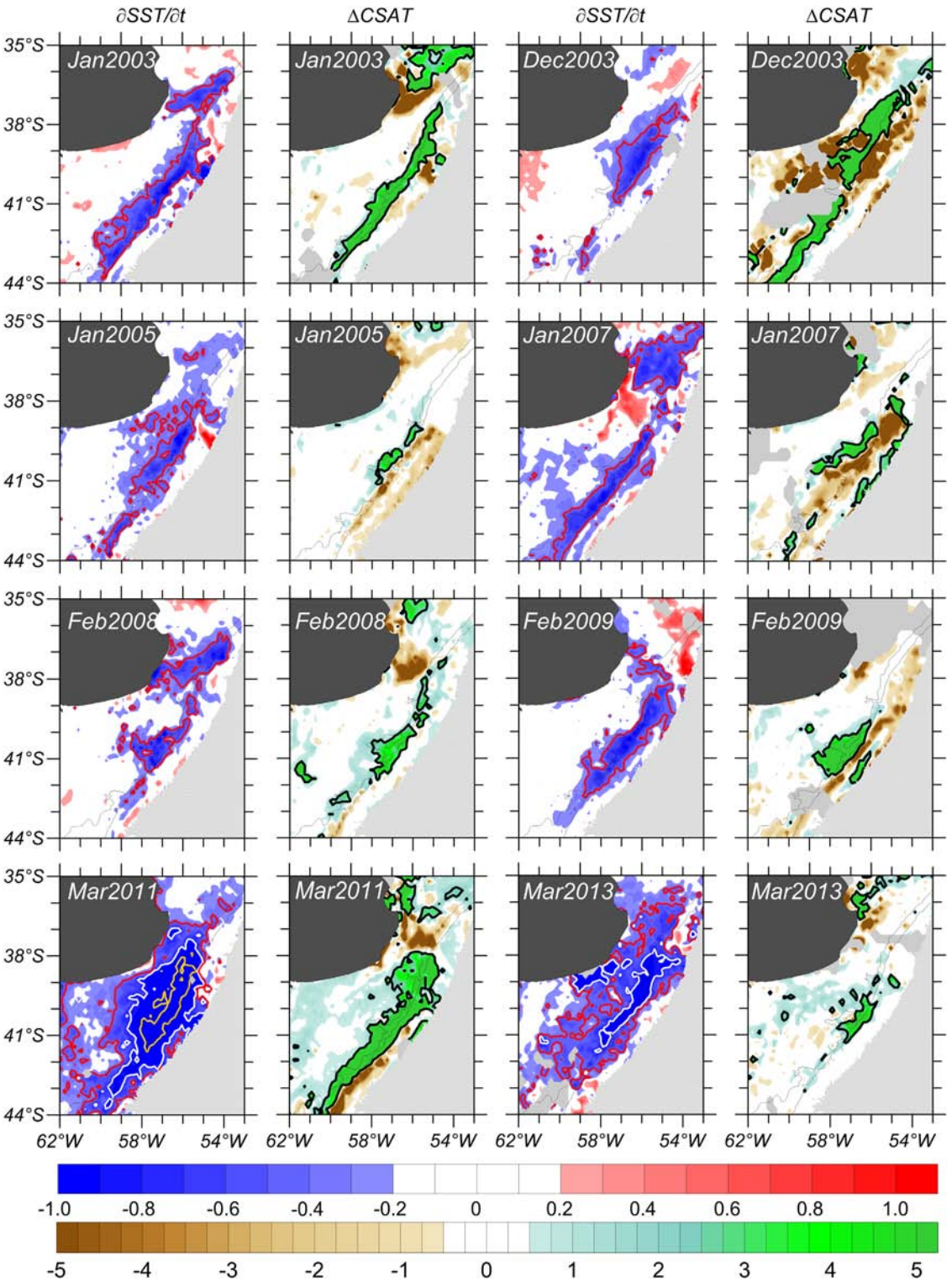

Figure 12. Rate of *SST* change ($\partial SST/\partial t$, °C d^{-1}) and surface chlorophyll difference over a 10 days period ($\Delta CSAT$, mg m^{-3}) during selected cooling events (see Table 4). Red, white and yellow contours indicate 0.4, 0.8, and 1.3°C d^{-1}, respectively. Heavy black contours indicate 2 mg m^{-3} differences. Depths greater than 2000 m are stippled for clarity. The light gray pixels indicate cloud-covered regions. The thin grey solid lines in all panels are the 100 and 200 m isobaths.

To determine which processes lead to the observed cooling, in addition to air-sea fluxes, horizontal advection and vertical advection are considered. To this end, we evaluate a simplified equation of temperature integrated over the mixed layer depth. Following the formalism proposed by *Vialard and Delecluse* [1998]:

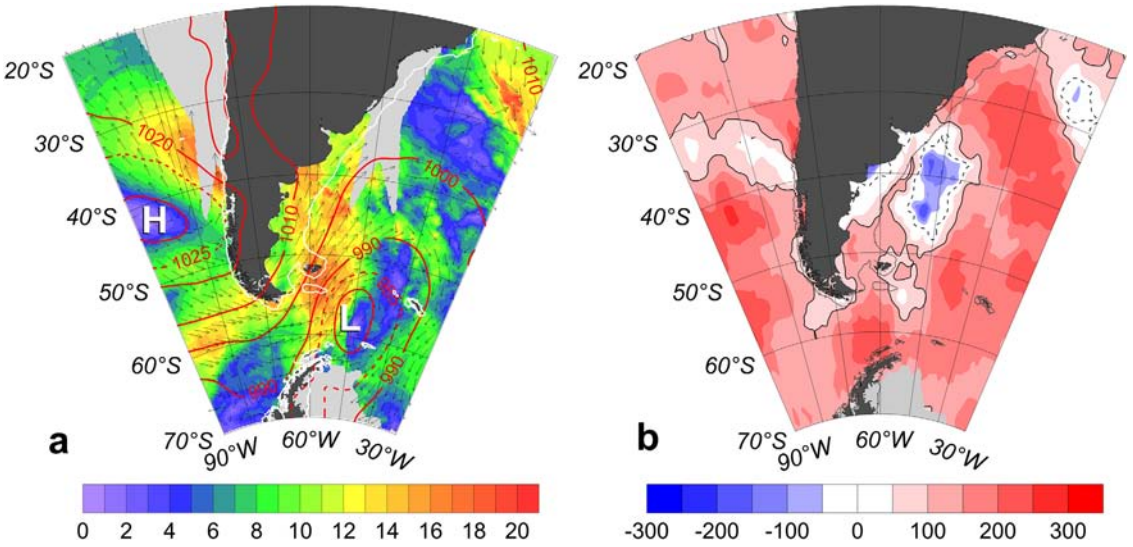

Figure 13. Atmospheric conditions during 13 January 2007 from CSFR (NCEP) and Quickscat. (a) Wind vectors and intensity (background colors in m s^{-1}) and surface pressure (red contours, hPa). Atmospheric high (H) and low (L) pressure centers are indicated. The solid white line is the 200 m isobath. (b) Net surface heat flux from OAFlux (W m^{-2}). The heavy dashed contour indicates zero flux and the gray solid contour represents the 100 W m^{-2} flux value. The solid black line is the 200 m isobath. Light gray shading in both panels indicates missing data due to either swath geometry or ice.

$$\frac{\partial T_m}{\partial t} + U_m \cdot \frac{\partial T_m}{\partial x} + V_m \cdot \frac{\partial T_m}{\partial y} + w_{-H}\left(\frac{T_m - T_{-H}}{H}\right) = \frac{Q_0}{\rho C_p H} \quad (1)$$

where x and y are the cross-shore and long-shore directions, T_m represents the mixed layer temperature, U_m and V_m represent the mixed layer cross-shore and long-shore velocities, respectively, Q_0 is the net heat flux through the sea surface, $\rho = 1022$ kg m^{-3} and $C_p = 3940$ J kg^{-1} °C^{-1} are the seawater density and specific heat, respectively, H is the mixed layer depth, and T_{-H} and w_{-H} are the temperature and vertical velocity at the base of the mixed layer, respectively. To derive equation (1), it is assumed that H is vertically and horizontally homogeneous and constant in time, the temperature and horizontal velocity within the mixed layer are vertically homogeneous, and the horizontal and vertical diffusivities are negligible. We assume $H = 10$ m, which is close to the mixed layer depth observed at site A (e.g., Figure 5). As mentioned above, the estimated net heat flux through the sea surface during 13–14 January at site B is positive (e.g., into the ocean, ~100 W m^{-2}). However, the net surface heat flux required to cause a 3°C temperature decrease in 2 days over a 10 m water column is approximately −700 W m^{-2}. Thus, whatever mechanism leads to the observed cooling it must also overcome the excess heat input through the sea surface. Note that using a deeper mixed layer implies a proportionally larger heat loss requirement (equation (1)). During the cooling period of 13–14 January, the average 10 m velocity observed at site B was almost in the long-shore direction ($U_m = 1$ cm s^{-1}; $V_m = 36$ cm s^{-1}). The estimated cross-shore SST gradient is $\partial T_m/\partial x \sim -3 \times 10^{-2}$°C km^{-1}, thus, the cross-shore temperature advection is estimated as $U_m \cdot \partial T_m/\partial x \sim -0.02$°C d^{-1}. According to equation (1), because $U_m > 0$, the cross-shore advection acts to warm the outer shelf region rather than cool it. The large reservoir of cold water located south of site B (e.g., Figure 8a) suggests that northeastward (long-shore) advection might contribute to the sharp cooling observed at that location. To estimate the long-shore temperature advection, we computed the long-shore temperature gradient from satellite SST $\partial T_m/\partial y \sim -2 \times 10^{-3}$°C km^{-1} following a constant ambient planetary potential vorticity contour passing over site B (2.2×10^{-7} m^{-1} s^{-1}) and over a distance of 200 km. Using these values, the long-shore temperature advection is $V_m \cdot \partial T_m/\partial y \sim 0.06$°C d^{-1}, which accounts for ~4% of the observed cooling rate. Moreover, given the observed long-shore SST gradients, for long-shore advection to fully account for the observed cooling rates, a long-shore velocity of 8.7 m s^{-1} would be required. To estimate the vertical heat advection, the vertical gradient in the third term of the right-hand side of equation (1) is estimated using the water column temperature data collected at site A. The averaged vertical temperature gradient at the base of the mixed layer for the last 30 days of the time series is $(T_{-m} - T_{-H})/H \approx 0.052$°C m^{-1}, where we use the temperature at 1 and 10 m depth to evaluate T_m and T_{-H}, respectively. Thus, neglecting all other terms in equation (1), the vertical velocity necessary to generate a temperature change of −1.5°C d^{-1} is

$w_{-H} \sim 29$ m d^{-1}. Though the implied vertical velocity is quite large, this estimate is in agreement with the results derived from realistic numerical simulations in the shelf break region [*Combes and Matano*, 2014]. Alternatively, we can use the higher vertical temperature gradient observed at station 64 in late March 2006 (Figure 3b, $(T_m - T_{-H})/H \approx 0.113$°C m^{-1}). The larger vertical temperature gradient requires a somewhat reduced, but still relatively large vertical velocity of $w_{-H} \sim 13$ m d^{-1}. We also estimated the Ekman pumping (w_E) at site B between 10 and 15 January 2007 based on the wind stress fields derived QuikSCAT surface winds (not shown). w_E is smaller than 1 m d^{-1} throughout this period, indicating that it does not significantly contribute the inferred vertical velocities. Thus, we conclude that shelf break upwelling is the most likely mechanism leading to the cooling observed in the outer shelf in January 2007.

There have been few attempts to estimate the vertical velocities associated with shelf break upwelling from direct observations, the majority of these studies were carried out off the Mid-Atlantic Bight. Based on the Lagrangian velocities inferred from the evolution of dye tracers injected within the bottom boundary layer, *Houghton* [1997] detected onshore flow on the offshore side of and close to the shelf break front south of Martha's Vineyard. This flow implies convergence within the bottom boundary layer and upwelling of near-bottom waters. A similar experiment yielded upwelling velocities of 4–7 m d^{-1} [*Houghton and Visbeck*, 1998]. This estimate is close to the 9 ± 2 m d^{-1} inferred from the distribution of suspended particles and by integrating the near-bottom horizontal velocity convergence observed during a high-resolution hydrographic, optical, and current survey at a nearby location [*Barth et al*., 1998]. Vertical velocity estimates were also derived from the analysis of the displacements of a neutrally buoyant float leading to a mean along-isopycnal vertical velocity of 17.5 m d^{-1} over a 2 day period, and maxima of 31 m d^{-1} between tidal cycles [*Barth et al*., 2004]. These observations in the Mid-Atlantic Bight are consistent with predictions of the detachment of the bottom boundary layer at the foot of the shelf break front based on numerical simulations [*Gawarkiewicz and Chapman*, 1992; *Chapman and Lentz*, 1994]. Recent simulations indicate that upwelling at the shelf break drives an interior secondary circulation and forms a shelf break jet [*Benthuysen et al*., 2015].

Numerical and analytical models suggest that other mechanisms may play a more significant role in generating upwelling along the PSB [*Matano and Palma*, 2008; *Miller et al*., 2011]. *Matano and Palma* [2008] argued that a combination of bottom friction and lateral diffusion in a slope current flowing in the direction of coastal trapped waves (e.g., with the coast at the left in the southern hemisphere) generates the onshore spreading of the slope current, leading to the development of an along shelf pressure gradient and divergence of the along shelf geostrophic velocity near the shelf break. The divergence of the along shelf flow leads to shelf break upwelling. The model also indicates that the intensity of upwelling is modulated by the strength of the slope current [see also *Miller et al*., 2011]. Our direct current observations show that the mid-January 2007 cooling event was associated with a coherent acceleration of the flow. Thus, maximum velocities ($>$60 cm s^{-1}) observed in the 60–80 m depth range and near bottom (160 m, $>$40 cm s^{-1}) may have enhanced the upwelling during the January 2007 event. The realistic high-resolution model of *Combes and Matano* [2014] shows that the time averaged vertical velocity presents intense, $\sim$50 km diameter, upwelling and downwelling cells distributed along the shelf break between 47°S and 39°S. Despite the complex spatial structure of the vertical velocity, the study also shows that its areal average along shelf break strip within the same latitude range is significantly correlated ($r = 0.66$) with the transport of the onshore portion of the MC. To assess the impact of upwelling at the shelf break in the model, *Combes and Matano* [2014] injected a virtual tracer along the shelf break at depths greater than 150 m between 46°S and 41.5°S and found the tracer emerged at the surface in the outer shelf northeast of the injection region (their Figure 19). The distribution of high tracer concentration in the model resembles the pattern of largest cooling revealed by the in situ and satellite observations described in section 3.3 (Figure 8c). Although our estimated vertical velocity are in agreement with the model results, we point out that the time scale required by the model to produce such an extensive area of upwelled tracer is significantly higher ($\sim$180 days) than the time scales observed in site B ($\sim$5 days).

The analysis of satellite-derived *SST* anomalies relative to the mean regional *SST* reveals 16 cooling events, including the event of January 2007 (Figure 11a). The duration of the events ranges from 3 to 18 days. Although it is not possible to evaluate the temperature advection during these events due to the lack of current observations, because long-shore *SST* gradients and cross-shore velocities are small, both long-shore and cross-shore advection appear to be too small to account for the observed cooling rates.

4.3. *CSAT* Response to Cooling Events

Cold events plausibly associated with shelf break upwelling may generate a nutrient flux that enhance phytoplankton growth over the outer continental shelf. Increased *CSAT* is observed after most of the cooling events when distributions of *SST* rate of change are available (Figure 12). Some of these events show a remarkable coincidence between areas of sharp cooling and increasing *CSAT* (e.g., January 2003 and February 2008). $\Delta CSAT$ maps also indicate enhanced chlorophyll *a* increase in the vicinity of 41°S during cold events, a region characterized by maximum nonseasonal surface chlorophyll variability [*Piola et al*., 2010]. Our results show that 75% of the analyzed cooling events are concurrent with a *CSAT* increase (Table 4). On average, the chlorophyll concentration increased 1.0 mg m^{-3} during the identified events, however, $\Delta CSAT$ values are highly variable between events. Moreover, events with similar cooling intensity exhibit opposite *CSAT* response. For example, during the December 2003 event, where $aSST = -1.97$°C, the observed *CSAT* increment was of 1 mg m^{-3}. On the other hand, the January 2007 event ($aSST = -2.28$°C) is associated with a *CSAT* decrease of 1.1 mg m^{-3}. During both events, NCEP and OAFLUX estimates of net heat flux were positive. The vertical structure of chlorophyll *a* does not seem to explain these differences. Vertical sections occupied north of site B (~39°S) in late spring and summer present a maximum chlorophyll *a* at the seasonal thermocline, which outcrops offshore [*Carreto et al*., 1995, Figures 2 and 8]. Thus, chlorophyll *a* is nearly homogeneous through the upper ~40 m of the water column offshore from the 100 m isobath, the region of largest observed cooling. A plausible explanation for such differences is that chlorophyll may respond to other environmental conditions, such as vertical stratification, and to different phytoplankton species present at the time of the event. Thus, similar cooling events may effectively promote or depress the response of phytoplankton.

5. Conclusions

Simultaneous in situ observations of temperature, salinity, and velocity profiles from two mooring deployments have been used to identify mechanisms leading to temperature variability in the northern Patagonian continental shelf break. Our results indicate that temperature and salinity fluctuations are not locally associated with either the cross-shore or the long-shore velocity component, except at semidiurnal frequencies at 75 and 100 m, thus implying a net offshore heat flux and onshore salinity flux below the thermocline. Our analyses indicate that the mean cross-shore heat flux below 80 m depth associated with the M_2 frequency represents 60% of the total mean cross-shore eddy heat flux. Significant coherence is observed between temperature and salinity at time periods longer than 18 hs, suggesting that cross-shelf exchanges between warm-fresh shelf water and cold-salty slope water occur at the shelf break.

Relatively intense and vertically coherent low-frequency *T* and *S* fluctuations are observed at both sites. The analysis of in situ temperature, salinity, and velocity data together with satellite-derived *SST* observations provided evidence of upwelling at the outer shelf and upper slope during a cold event recorded in January 2007. *SST* data indicate that the decrease in surface temperature extended ~500 km along the outer shelf. By evaluating a simplified temperature balance at the mooring site, we found that neither the cross-shore exchanges nor the heat exchanges between the atmosphere and the ocean account for the observed cooling rate. Instead, a vertical velocity of 29 m d^{-1} is necessary to sustain the recorded decrease in surface temperature. This value is in agreement with vertical velocities estimated in recent realistic numerical simulations in the shelf break region. The vertically coherent acceleration of the long-shore flow observed during the cooling event is also in agreement with numerical model results, which suggest a positive correlation between the intensity of the shelf break upwelling and the strength of the onshore portion of the MC.

Other cooling events over the outer shelf and shelf break were detected as nonseasonal *SST* anomalies minima. These events are also characterized by enhanced cooling in the shelf break region, and given the observed surface heat flux exchange with the atmosphere, it is likely that shelf break upwelling events account for the observed decrease in *SST*. The impact of the upwelling events on nutrient enrichment was also analyzed using *CSAT* as a proxy for biomass growth. Our results show that 75% of the analyzed cooling events are concurrent with a *CSAT* increase over a period of 5 days after the cooling events. Moreover, some of these events show a remarkable coincidence between areas of sharp cooling and increasing *CSAT*. Nevertheless, differences in *CSAT* response suggest that phytoplankton communities respond differently to similar cooling events. In summary, our results indicate that shelf break upwelling is in large part

responsible of the observed cooling events and subsequent nutrient enrichment processes on the PSB. Continuous measurements of currents and physical properties and dedicated physical-biogeochemical models will be essential to obtain a better understanding of the Patagonian shelf break dynamics and its interaction with the local ecosystem.

Acknowledgments

The hydrographic data are available at http://data.nodc.noaa.gov/cgi-bin/iso?id=gov.noaa.nodc:0110317 and http://www.nodc.noaa.gov/OC5/WOD/pr_wod.html. *SST* and MODIS Aqua data are available at http://oceancolor.gsfc.nasa.gov. Daily net surface heat fluxes are available at http://oaflux.whoi.edu/ and http://www.esrl.noaa.gov/-psd/data/gridded/data.ncep.reanalysis.html. The time series data at sites A and B will be submitted to NODC. This research was funded by grant CRN3070 from the Inter-American Institute for Global Change Research, which is supported by the US National Science Foundation (grant GEO-1128040). Additional funding was provided by Universidad de Buenos Aires (UBACyT08-10 X176) and MinCyT/CONAE grant 001. D.V. was supported by a fellowship from Consejo Nacional de Investigaciones Científicas y Técnicas, Argentina. Discussions with Elbio Palma, Ricardo Matano, and Vincent Combes and comments from two anonymous reviewers are gratefully acknowledged.

References

Acha, E. M., H. W. Mianzán, R. A. Guerrero, M. Favero, and J. Bava (2004), Marine fronts at the continental shelves of austral South America, physical and ecological processes, *J. Mar. Syst.*, *44*(1–2), 83–105.

Barth, J. A., D. Bogucki, S. D. Pierce, and P. M. Kosro (1998), Secondary circulation associated with a shelfbreak front, *Geophys. Res. Lett.*, 15, 2761–2764, doi:10.1029/98GL02104.

Barth, J. A., D. Hebert, A. C. Dale, and D. S. Ullman (2004), Direct observations of along-isopycnal upwelling and diapycnal velocity at a shelf-break front, *J. Phys. Oceanogr.*, *34*, 543–565.

Benthuysen, J., L. Thomas, and S. Lentz (2015), Rapid generation of upwelling at a shelf break caused by buoyancy shutdown, *J. Phys. Oceanogr.*, *45*, 294–312.

Bianchi, A. A., L. Bianucci, A. R. Piola, D. Ruiz Pino, I. Schloss, A. Poisson, and C. F. Balestrini (2005), Vertical stratification and sea-air CO_2 fluxes in the Patagonian shelf, *J. Geophys. Res.*, *110*, C07003, doi:10.1029/2004JC002488.

Bianchi, A. A., D. Ruiz-Pino, H. Isbert Perlender, A. P. Osiroff, V. Segura, V. A. Lutz, M. Luz Clara, C. F. Balestrini, and A. R. Piola (2009), Annual balance and seasonal variability of sea-air CO_2 fluxes in the Patagonia Sea: Their relationship with fronts and chlorophyll distribution, *J. Geophys. Res.*, *114*, C03018, doi:10.1029/2008JC004854.

Bisbal, G. (1995), The Southeast South American shelf large marine ecosystem: Evolution and components, *Mar. Policy*, *19*, 21–38.

Bogazzi, E., A. Baldoni, A. Rivas, P. Martos, R. Reta, J. M. Orensanz, M. Lasta, P. Dell'Arciprete, and F. Werner (2005), Spatial correspondence between areas of concentration of Patagonian scallop (*Zygochlamys patagonica*) and frontal systems in the southwestern Atlantic, *Fish. Oceanogr.*, *14*(5), 359–376.

Boyer, T. P., et al. (2013), World Ocean Database 2013, in *NOAA Atlas NESDIS 72*, edited by S. Levitus and A. Mishonov, 209 pp., Silver Spring, Md.

Carreto, J. I., V. A. Lutz, M. O. Carignan, A. D. Cucchi Colleoni, and S. G. de Marco (1995), Hydrography and chlorophyll a in a transect from the coast to the shelf-break in the Argentinian Sea, *Cont. Shelf Res.*, *15*, 315–336.

Chapman, D. C., and S. J. Lentz (1994), Trapping of a coastal density front by the bottom boundary layer, *J. Phys. Oceanogr.*, *24*(7), 1464–1479.

Charo, M., and A. R. Piola (2014), Hydrographic data from the GEF Patagonia cruises, *Earth Syst. Sci. Data*, *6*, 265–271.

Combes, V., and R. P. Matano (2014), A two-way nested simulation of the oceanic circulation in the Southwestern Atlantic, *J. Geophys. Res. Oceans*, *119*, 731–756, doi:10.1002/2013JC009498.

Falabella, V., C. Campagna, and J. Croxall (Eds.) (2009), *Atlas del Mar Patagónico. Especies y Espacios*, Wildlife Conserv. Soc. and Birdlife Int., Buenos Aires.

Franco, B. C., A. R. Piola, A. L. Rivas, A. Baldoni, and J. P. Pisoni (2008), Multiple thermal fronts near the Patagonian shelf break, *Geophys. Res. Lett.*, *35*, L02607, doi:10.1029/2007GL032066.

Garcia, V. M. T., C. A. E. Garcia, M. M. Mata, R. Pollery, A. R. Piola, S. Signorini, C. R. McClain, and M. D. Iglesias-Rodríguez (2008), Environmental factors controlling the phytoplankton blooms at the Patagonia shelfbreak in spring, *Deep Sea Res., Part I*, *55*, 1150–1166.

Garreaud, R. (1999), Cold air incursions over Subtropical and Tropical South America: A case study, *Mon. Weather Rev.*, *127*, 2823–2853.

Garreaud, R. (2000), Cold air incursions over Subtropical and Tropical South America: Mean structure and dynamics, *Mon. Weather Rev.*, *128*, 2544–2559.

Gawarkiewicz, G., and D. C. Chapman (1992), The role of stratification in the formation and maintenance of shelf-break fronts, *J. Phys. Oceanogr.*, *22*(7), 753–772.

Guerrero, R. A., and A. R. Piola (1997), Masas de agua en la Plataforma Continental, in *El Mar Argentino y sus Recursos Pesqueros*, vol. 1, edited by E. Boschi, pp. 107–118, Inst. Nac. de Invest. y Desarrollo Pesquero, Mar del Plata, Argentina.

Heileman S. (2009), XVI-55 Patagonian Shelf LME, in *The UNEP Large Marine Ecosystem Report: A Perspective on Changing Conditions in LMEs of the World's Regional Seas*, edited by K. Sherman and G. Hempel, *UNEP Reg. Seas Rep. and Stud. 182*, pp. 735–746, U. N. Environ. Programme, Nairobi.

Houghton, R. W. (1997), Lagrangian flow at the foot of a shelfbreak front using a dye tracer injected into the bottom boundary layer, *Geophys. Res. Lett.*, *24*, 2035–2038, doi:10.1029/97GL02000.

Houghton, R. W., and M. Visbeck (1998), Upwelling and convergence in the Middle Atlantic Bight Shelfbreak Front, *Geophys. Res. Lett.*, *25*, 2765–2768, doi:10.1029/98GL02105.

IOC, IHO, and BODC (2003), "Centenary Edition of the GEBCO Digital Atlas", published on CD-ROM on behalf of the Intergovernmental Oceanographic Commission and the International Hydrographic Organization as part of the General Bathymetric Chart of the Oceans; British Oceanographic Data Centre, Liverpool.

Kalnay, E., et al. (1996), The NCEP/NCAR 40-year reanalysis project, *Bull. Am. Meteorol. Soc.*, *77*, 437–470.

Longhurst, A. (1998), *Ecological Geography of the Sea*, Academic, San Diego, Calif.

Lutz, V. A., V. Segura, A. I. Dogliotti, D. A. Gagliardini, A. A. Bianchi, and C. F. Balestrini (2010), Primary production in the Argentine Sea during spring estimated by field and satellite models, *J. Plankton Res.*, *32*, 181–195.

Matano, R. P. (1993), On the separation of the Brazil Current from the coast, *J. Phys. Oceanogr.*, *23*(1), 79–90.

Matano, R. P., and E. D. Palma (2008), On the upwelling of downwelling currents, *J. Phys. Oceanogr.*, *38*(11), 2482–2500.

Matano, R. P., E. D. Palma, and A. R. Piola (2010), The influence of the Brazil and Malvinas Currents on the southwestern Atlantic shelf circulation, *Ocean Sci.*, *6*, 983–995.

Miller, R. N., R. P. Matano, and E. D. Palma (2011), Shelfbreak upwelling induced by alongshore currents: Analytical and numerical results, *J. Fluid Mech.*, *686*, 239–249.

Muller-Karger, F. E., R. Varela, R. Thunell, R. Luerssen, C. Hu, and J. J. Walsh (2005), The importance of continental margins in the global carbon cycle, *Geophys. Res. Lett.*, *32*, L01602, doi:10.1029/2004GL021346.

O'Reilly, J. E., et al. (2000), *SeaWiFS Postlaunch Calibration and Validation Analyses, Part 3, SeaWiFS Postlaunch Tech. Rep. Ser.*, vol. 11, edited by S. B. Hooker and R. E. Firestone, *NASA Tech. Memo. 2000-206892*, NASA, Goddard Space Flight Cent., Greenbelt, Md.

Palma, E. D., and R. P. Matano (2012), A numerical study of the Magellan Plume, *J. Geophys. Res.*, *117*, C05041, doi:10.1029/2011JC007750.

Palma, E. D., R. P. Matano, and A. R. Piola (2004), A numerical study of the Southwestern Atlantic Shelf circulation: Barotropic response to tidal and wind forcing, *J. Geophys. Res.*, *109*, C08014, doi:10.1029/2004JC002315.
Palma, E. D., R. P. Matano, and A. R. Piola (2008), A numerical study of the Southwestern Atlantic Shelf circulation: Stratified ocean response to local and offshore forcing, *J. Geophys. Res.*, *113*, C11010, doi:10.1029/2007JC004720.
Peterson, R. G., and T. Whitworth (1989), The Subantarctic and Polar Fronts in relation to deep water masses through the southwestern Atlantic, *J. Geophys. Res.*, *94*, 10,817–10,838, doi:10.1029/JC094iC08p10817.
Piola, A. R., and A. L. Gordon (1989), Intermediate waters in the southwest South Atlantic, *Deep Sea Res., Part A*, *36*(1), 1–16.
Piola, A. R., and R. P. Matano (2001), The South Atlantic Western Boundary Currents Brazil/Falkland (Malvinas) Currents, in *Encyclopedia of Ocean Sciences*, vol. 1, edited by J. M. Steele, S. A. Thorpe, and K. K. Turekian, pp. 340–349, Academic Press, Boston, Mass.
Piola, A. R., N. Martinez Avellaneda, R. A. Guerrero, F. P. Jardón, E. D. Palma, and S. I. Romero (2010), Malvinas-slope water intrusions on the northern Patagonia, *Ocean Sci.*, *6*, 345–359.
Piola, A. R., B. C. Franco, E. D. Palma, and M. Saraceno (2013), Multiple jets in the Malvinas Current, *J. Geophys. Res. Oceans*, *118*, 2107–2117, doi:10.1002/jgrc.20170.
Podestá, G. P. (1997), Utilización de datos satelitarios en investigaciones oceanográfica y pesqueras en el Océano Atlántico Sudoccidental, in *El mar argentino y sus Recursos Pesqueros*, vol. 1, edited by E. E. Boschi., pp. 195–222, Inst. Nac. de Invest. y Desarrollo Pesquero, Mar del Plata, Argentina.
Reynolds, R. W., T. M. Smith, C. Liu, D. B. Chelton, K. S. Casey, and M. G. Schlax (2007), Daily high-resolution-blended analyses for sea surface temperature, *J. Clim.*, *20*, 5473–5496.
Rivas, A. L. (1997), Current meter observations in the Argentine Continental Shelf, *Cont. Shelf Res.*, *17*, 391–406.
Rivas, A. L., and A. R. Piola (2002), Vertical stratification at the shelf off northern Patagonia, *Cont. Shelf Res.*, *22*, 1549–1558.
Rivas, A. L., and J. P. Pisoni (2010), Identification, characteristics and seasonal evolution of surface thermal fronts in the Argentinean Continental Shelf, *J. Mar. Syst.*, *79*, 134–143.
Rodhouse, P. G., C. D. Elvidge, and P. N. Trathan (2001), Remote sensing of the global light-fishing fleet: An analysis of interactions with oceanography, other fisheries and predators, *Adv. Mar. Biol.*, *39*, 261–303.
Romero, S. I., A. R. Piola, M. Charo, and C. A. E. Garcia (2006), Chlorophyll-a variability off Patagonia based on SeaWiFS data, *J. Geophys. Res.*, *111*, C05021, doi:10.1029/2005JC003244.
Saha, S., et al. (2010), The NCEP Climate Forecast System Reanalysis, *Bull. Am. Meteorol. Soc.*, *91*(8), 1015–1057.
Sánchez, R. P., and J. D. Ciechomski (1995), Spawning and nursery grounds of pelagic fish species in the sea-shelf off Argentina and adjacent areas, *Sci. Mar.*, *59*, 455–478.
Saraceno, M., C. Provost, A. R. Piola, J. Bava, and A. Gagliardini (2004), Brazil Malvinas Frontal System as seen from 9 years of advanced very high resolution radiometer data, *J. Geophys. Res.*, *109*, C05027, doi:10.1029/2003JC002127.
Signorini, S. R., V. M. T. Garcia, A. R. Piola, H. Evangelista, C. R. McClain, C. A. E. Garcia, and M. M. Mata (2009), Further studies on the physical and biogeochemical causes for large interannual changes in the Patagonian shelf spring–summer phytoplankton bloom biomass, *NASA Tech. Memo. NASA/TM-2009-214176*, NASA, Greenbelt, Md.
Spadone, A., and C. Provost (2009), Variations in the Malvinas Current volume transport since October 1992, *J. Geophys. Res.*, *114*, C02002, doi:10.1029/2008JC004882.
Vialard, J., and P. Delecluse (1998), An OGCM Study for the TOGA Decade. Part I: Role of Salinity in the Physics of the Western Pacific Fresh Pool, *J. Phys. Oceanogr.*, *28*, 1071–1088.
Vivier, F., and C. Provost (1999), Direct velocity measurements in the Malvinas Current, *J. Geophys. Res.*, *104*, 21,083–21,103, doi:10.1029/1999JC900163.
Walsh, J. J. (1991), Importance of continental margins in the marine biogeochemical cycling of carbon and nitrogen, *Nature*, *350*, 53–55.
Yu, L., and R. A. Weller (2007), Objectively analyzed air-sea heat fluxes for the global ice-free oceans (1981–2005), *Bull. Am. Meteorol. Soc.*, *88*, 527–539.
Yu, L., X. Jin, and R. A. Weller (2008), Multidecade Global Flux Datasets from the Objectively Analyzed Air-sea Fluxes (OAFlux) Project: Latent and sensible heat fluxes, ocean evaporation, and related surface meteorological variables, *OAFlux Proj. Tech. Rep. OA-2008-01*, 64 pp., Woods Hole Oceanogr. Inst., Woods Hole, Mass.